

# Mg and Sr isotopic evidence for basin wide alteration of early diagenetic dolomite in the Williston Basin by ascending crustal fluids

Sara R. Kimmig<sup>a,b,\*</sup>, Matthew D. Nadeau<sup>a,c</sup>, Peter K. Swart<sup>d</sup>, Chris Holmden<sup>a</sup>

<sup>a</sup> University of Saskatchewan, Saskatchewan Isotope Laboratory, Department of Geological Sciences, Saskatoon, SK S7N 5E2, Canada

<sup>b</sup> Pennsylvania State University, Laboratory for Isotopes and Metals in the Environment (LIME), Earth and Environmental Systems Institute, University Park, PA 16802, USA

<sup>c</sup> Princeton University, Department of Geosciences, Guyot Hall, Princeton, NJ 08544, USA

<sup>d</sup> University of Miami, Department of Marine Geosciences, Rosenstiel School of Marine and Atmospheric Sciences, Miami, FL 33149, USA

Received 29 August 2020; accepted in revised form 3 June 2021; available online 10 June 2021

## Abstract

Dolomite is a predominantly diagenetic mineral that forms by replacing marine calcite and aragonite during burial. Dolomitization requires subsurface fluid flow to deliver Mg and remove product Ca, and only forms abiotically in laboratory experiments at temperatures above ~100°C, equivalent to burial depths of 3 km or greater. Limited sources of Mg at these depths would appear to restrict most dolomite formation to shallow burial depths using seawater as a source of reactive Mg, despite the kinetic limitation imposed by lower temperatures. The Williston Basin is replete with evaporites and dolomites that appear to have formed using Mg from evaporatively concentrated seawater at near surface temperatures. However, two dolomite bodies examined in this study record basin wide gradients in  $^{87}\text{Sr}/^{86}\text{Sr}$  ratios and  $\delta^{26}\text{Mg}$  values that are inconsistent with dolomitization by seawater. We evaluate the processes that may have created these gradients. We propose a model whereby seepage reflux created early diagenetic protodolomite that was later altered during deep burial by  $^{87}\text{Sr}$  and Mg-enriched fluids ascending from the deep structural center of the basin with the degree of alteration decreasing towards the edges. The ascending fluid flow event is tentatively linked to anomalous heating in the Late Devonian / Early Carboniferous. Vertical faults are hypothesized to have behaved as conduits for channeling  $^{87}\text{Sr}$  and Mg-enriched crustal fluids upwards into the bottom of the Williston Basin, pressurizing the basal aquifer system and commencing up-dip directed fluid flow through confined aquifers. Clumped isotope and fluid inclusion thermometry indicate that the ascending fluids were hydrothermal with an estimated  $\delta^{26}\text{Mg}$  value of  $-0.65 \pm 0.20\text{‰}$ , which is much lower than estimates of early Paleozoic seawater  $\delta^{26}\text{Mg}$  values of  $+0.09$  to  $+0.23\text{‰}$ . Two sources of crustal Mg are consistent with the low inferred  $\delta^{26}\text{Mg}$  values of the ascending fluid: (1) chlorite, which preferentially releases isotopically light Mg, with literature values in the range  $-0.78\text{‰}$  to  $-1.8\text{‰}$ , and (2) magnesite, which forms during carbonation of serpentinite with literature values in the range  $-0.7\text{‰}$  to  $-1.1\text{‰}$ . Ultramafic rocks belonging to the Thompson Nickel Belt pass beneath the center of the Williston Basin in North Dakota, indicating that dissolution of both chlorite and magnesite may have contributed reactive Mg to the Williston Basin during the ascending fluid flow event. As dolomite is a mineral that is easily altered during burial, our findings warrant caution in choosing dolomites for reconstructing the  $^{26}\text{Mg}$  history of seawater.

© 2021 Elsevier Ltd. All rights reserved.

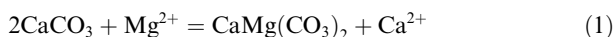
\* Corresponding author at: Pennsylvania State University, Laboratory for Isotopes and Metals in the Environment (LIME), Earth and Environmental Systems Institute, University Park, PA 16802, USA.

E-mail addresses: [srkimmig@psu.edu](mailto:srkimmig@psu.edu) (S.R. Kimmig), [matthew.nadeau@princeton.edu](mailto:matthew.nadeau@princeton.edu) (M.D. Nadeau), [pswart@rsmas.miami.edu](mailto:pswart@rsmas.miami.edu) (P.K. Swart), [chris.holmden@usask.ca](mailto:chris.holmden@usask.ca) (C. Holmden).

**Keywords:** Dolomite; Magnesium isotopes; Strontium isotopes; Clumped isotopes; Sedimentary basins; Paleohydrology; Hydrogeochemistry

## 1. INTRODUCTION

Large dolomite bodies require subsurface fluid flow to deliver reactive Mg to the sites of dolomitization and remove product Ca (Eq. (1)).



Seawater features prominently in hydrogeological models of dolomitization due to the large oceanic inventory of Mg. Differences in salinity (brine reflux) (Adams and Rhodes, 1960), temperature (Kohout convection) (Kohout, 1967), and hydraulic head create pressure gradients that drive seawater through shallowly buried carbonate sediment (Simms, 1984). In deeper burial environments, formation waters migrate in response to fluid-pressure gradients caused by sediment compaction (Illing, 1959), tectonic loading (Oliver, 1986), topographically-driven meteoric water recharge (Tóth, 1978), and heating by magmatic intrusions (Wilson et al., 1990) (Fig. S1). Although dolomite is known to form more efficiently at higher temperatures, the volume of dolomite produced in deep burial environments is assumed to be limited by the scarcity of deep sources of reactive Mg.

Despite repeated demonstrations from laboratory studies showing that dolomite should not form abiotically in near surface environments at ambient Earth surface temperatures (Sibley et al., 1994; Land, 1998; Arvidson and MacKenzie, 1999), most replacive dolomite in the rock record is still believed to form before deeper burial severs the hydrologic connectivity between seawater and subsurface sites of dolomitization (Land, 1980; Morrow, 1982; Warren, 2000; Machel, 2004; Gregg et al., 2015). This early diagenetic formation of dolomite is supported by deposits beneath carbonate platforms in the modern oceans such as the Bahamas and Cayman Islands (Vahrenkamp and Swart, 1990, 1994; Jones and Luth, 2002). However, the volume of dolomite is very small compared to the volume of carbonate sediment composed of aragonite and calcite. In some cases, ‘background dolomite’ in these settings can be related to the structural rearrangement of high magnesium calcite (HMC) (Murray et al., 2020), lessening the requirement for subsurface fluid flow to deliver large quantities of Mg. In fact, laboratory studies have shown that it is not even dolomite that initially precipitates by Eq. (1), but rather a very high magnesium calcite (VHMC) or Ca-rich ‘protodolomite’, that is more soluble than stoichiometric dolomite (molar Mg/Ca ratio  $\approx 1$ ) with ideal cation ordering (Sibley et al., 1994; Gregg et al., 2015). Most of the ‘island dolomite’ that formed in the Cenozoic is protodolomite (Jones and Luth, 2002; Ren and Jones, 2017). By contrast, true crystallographic dolomite is mostly found in older marine carbonates in sedimentary basins (Hardie, 1987; Kaczmarek and Sibley, 2011), indicating a propensity for metastable protodolomite to convert to dolomite during burial.

Sedimentary basins are low areas of the crust of tectonic origin where sediment accumulates. When the seas were high, sedimentary basins on the continents accrued greater thicknesses of marine sediment compared to surrounding regions. Subsidence protected these sedimentary deposits from erosion when the seas retreated. Over geological time, the sedimentary rock record became increasingly relegated to sedimentary basins that were actively subsiding in different geological periods. Several features have likely contributed to the large quantities of dolomite found in sedimentary basins. Firstly, in epicontinental marine settings, climate, sea level and circulation-restrictions create local conditions that may concentrate Mg by increasing the rate of seawater evaporation and its Mg/Ca ratio in areas of evaporite (anhydrite) deposition, thus making shallow burial dolomitization more efficient by Eq. (1). Secondly, evaporatively concentrated seawater creates hydraulic (density) head for driving subsurface fluid flow in underlying carbonates (Adams and Rhodes, 1960; Simms, 1984; Shields and Brady, 1995). Thirdly, dolomitization is more efficient at higher temperatures found in deep burial environments. Lastly, sedimentary basins form in tectonically active regions of the crust where fracture-networks and vertical faults provide conduits for passing hot and potentially Mg-bearing fluids upwards from the crust into the basal aquifer systems of sedimentary basins. This study brings new data to bear on the importance of the crust as a source of fluid and Mg for driving dolomitization during deep burial in sedimentary basins.

Episodic tectonism and anomalous heating create opportunities for subsurface fluid flow in sedimentary basins, lengthening the history of water–rock interactions that may contribute to the alteration of early diagenetic protodolomite, and creating opportunities for the formation of new dolomite by replacement of aragonite and calcite. Because fluid flow is implied in either case, gradients in the geochemistry of subsurface dolomite bodies may reveal directions of migrating paleofluids in sedimentary basins. Several influential studies have been published over the years using the stable isotopes of O and C, concentrations of Mn and rare earth elements, and  $^{87}\text{Sr}/^{86}\text{Sr}$  ratios in dolomite (Machel and Anderson, 1989; Banner and Hanson, 1990; Wilson et al., 1990; Qing and Mountjoy, 1992, 1994; Montañez, 1994; Nielsen et al., 1994). Hydrogeological models of dolomitization picture Mg-bearing fluids moving in response to pressure-gradient forces (Fig. S1). Knowledge of fluid flow directions can help to select the best model of dolomitization, and pinpoint the source of reactive Mg.

In this study, we use  $^{26}\text{Mg}/^{24}\text{Mg}$  ratios (presented as  $\delta^{26}\text{Mg}$  values) to directly trace the origin of the Mg-bearing fluids that formed two basin wide dolomite bodies in the Williston Basin, consisting of: (1) dolomitized sediment infilling a network of interconnected *Thalassinoides* burrows in the Late Ordovician Red River Formation,

and (2) replace matrix dolomite in the Middle Devonian Lower Member Winnipegosis Formation. Dolomite preferentially sequesters light isotopes of Mg during its formation (Galy et al., 2002; Higgins and Schrag, 2010; Fantle and Higgins, 2014; Li et al., 2015; Geske et al., 2015; Kimmig and Holmden, 2017; Higgins et al., 2018), thus leaving the residual pool of reactive Mg isotopically heavier. As a result, Mg in the fluid and dolomite may, under some conditions, become isotopically heavier in the direction of fluid flow (Peng et al., 2016; Ahm et al., 2018; Nadeau et al., 2019). Alternatively, as early diagenetic protodolomite is susceptible to Mg-exchange with fluids during burial, dolomite bodies may also preserve geochemical gradients that reflect a change from fluid-buffered to sediment-buffered diagenetic conditions along the fluid flow path, rather than formation of new dolomite (or protodolomite) by replacing calcite or aragonite.

The Red River and Winnipegosis dolomites are both overlain by evaporites, indicating that evaporatively concentrated seawater could have supplied all of the Mg for dolomitization. Yet, previous work on cores from a few locations in the Williston Basin has shown that both dolomite bodies record  $^{87}\text{Sr}/^{86}\text{Sr}$  ratios that are closer to present day deeply buried formation waters than seawater in the Late Ordovician and Middle Devonian (Qing et al., 2001; Fu et al., 2006). These findings are seemingly inconsistent with dolomitization by evaporatively concentrated seawater, suggesting that they were instead formed, or altered, by fluids encountered during burial. To improve understanding of the origin and significance of dolomite with high  $^{87}\text{Sr}/^{86}\text{Sr}$  ratios in the Williston Basin, we increased the geographic coverage of the sampled cores and measured both  $^{87}\text{Sr}/^{86}\text{Sr}$  ratios and  $\delta^{26}\text{Mg}$  values with the aim of determining whether mappable isotopic gradients exist within the two dolomite bodies that could yield clues regarding the source of the  $^{87}\text{Sr}$ -enriched fluids and their capacity for dolomitization. In addition, we present clumped isotope analyses ( $\Delta_{47}$  values) of selected dolomites to determine paleotemperatures of dolomite formation and the  $\delta^{18}\text{O}$  values of the migrating fluids.

## 2. GEOLOGY, HYDROSTRATIGRAPHY AND GEOCHEMISTRY OF DOLOMITE IN THE WILLISTON BASIN BELOW THE PRAIRIE EVAPORITE

The Williston Basin is an intracratonic sedimentary basin underlying parts of Saskatchewan, Manitoba, Montana, North Dakota, and South Dakota that preserves a ~4.9 km maximum thickness of mostly marine sediments of Cambrian to Cretaceous age (Kuhn et al., 2012). The structural center of the basin is located near Williston, North Dakota (Fig. 1b, c). The lowermost ~1.1 km underlying the ~200 m thick Middle Devonian Prairie Evaporite Formation is the subject of this study. Here there are four hydrostratigraphic units capable of channeling subsurface fluid flow, including: the Cambrian-Ordovician Deadwood Formation and Winnipeg Formation sandstones (Unit 1); the Late Ordovician Red River Group (Unit 2); the Ordovician-Silurian Interlake, Stonewall, and Stony

Mountain formations (Unit 3); and the Winnipegosis Formation (Unit 4) (Fig. 2; Bachu and Hitchon, 1996; Iampen and Rostron, 2000). The hydrostratigraphic units are carbonates, except for the basal aquifer which is sandstone. Shale aquitards or evaporite aquicludes separate and confine the aquifers: (1) the Winnipeg shales separate the Deadwood sandstone from the overlying Red River carbonate; (2) the 'A', 'B' and 'C' member carbonates of the Red River are each partially overlain by bedded anhydrites; (3) shale of the Ashern Formation separates the Interlake, Stonewall, and Stony Mountain carbonates from those of the Winnipegosis; and (4) the Prairie Evaporite aquiclude caps the whole sequence (Fig. 2). Dolomite bodies at the top and bottom of the succession, represented by the 'C' Member of the Red River (Unit 2) and Lower Member Winnipegosis (Unit 4), respectively, were selected for this study. These dolomite bodies are stratigraphically separated by ~550 m in the center of the Williston Basin and ~200 m near the edges (Burrus et al., 1996).

### 2.1. Red River Formation

The 'C' Member carbonate is ~100–150 m thick (Kohm and Loudon, 1978). It is characterized by a conspicuous network of anastomosing shrimp-like *Thalassinoides* burrows comprising ~50% of the unit by volume (Fig. S2b, c—photo of Tyndall Stone—a popular Red River facing stone) (Kendall, 1976; Gingras et al., 2004; Jin et al., 2012). It is common for the burrows to be fully dolomitized and for the matrix carbonate to be preserved as limestone (Figs. S2–S3), though in some locations the matrix and burrows are both dolomitized. The 'C' Member carbonate underlies bedded anhydrite of the Herald Formation. The 'A' and 'B' member carbonates are also overlain by anhydrite, and together with the 'C' Member, they are interpreted to represent three brining upward sequences (Longman and Haidl, 1996), reflecting three episodes of basin restriction in the Late Ordovician. The anhydrite is interpreted to have precipitated subaqueously from evaporatively concentrated seawater that was supersaturated with respect to gypsum (Longman et al., 1983), or in a playa-like environment characterized by repeated wetting and drying cycles (Kendall, 1984). Selective dolomitization of the burrows has been attributed to either Mg-rich brines that filtered downward from overlying evaporite basins with the burrows serving as conduits that channelized fluid flow (Kendall, 1976, 1977; Longman et al., 1983; Longman and Haidl, 1996), or microbially-mediated dolomitization of the burrow fill (Gingras et al., 2004). Lithological descriptions and selected petrographic analysis of the Red River carbonates may be found in numerous publications (Kendall, 1976, 1977; Kohm and Loudon, 1978; Longman et al., 1983; Longman and Haidl, 1996; Zenger, 1996; Qing et al. 2001; Pu and Qing, 2003; Gingras et al., 2004; Pratt and Haidl, 2008; Jin et al., 2012; Husinec, 2016).

Qing et al. (2001) studied dolomites of the Red River using two cores collected from wells drilled in southern Saskatchewan. They described three types of dolomite in the 'C' Member: (1) replacement of the carbonate sediment infilling the *Thalassinoides* burrows, (2) replacement of the

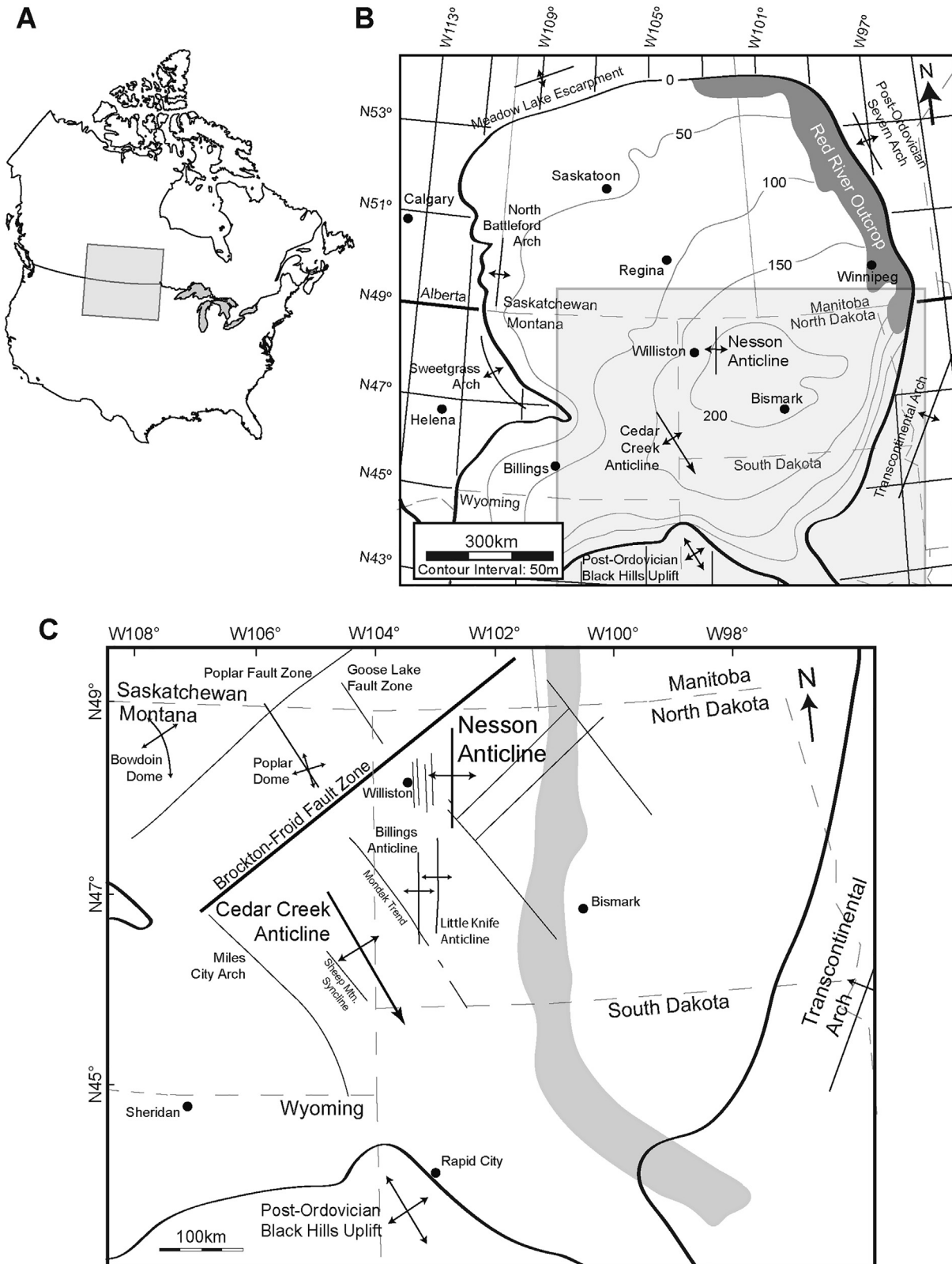


Fig. 1. A) Location of the Williston Basin in North America. B) Isopach map of the Red River Formation in the Williston Basin. The center of basin is in northeastern North Dakota (figures modified from Longman and Haidl (1996) and Pratt and Haidl (2008)). C) Faults and other structural features of the crust underlying the center of the Williston Basin. Thompson Nickel Belt is depicted in gray shading (Klasner and King, 1986) (figure modified from Anna, 2013).



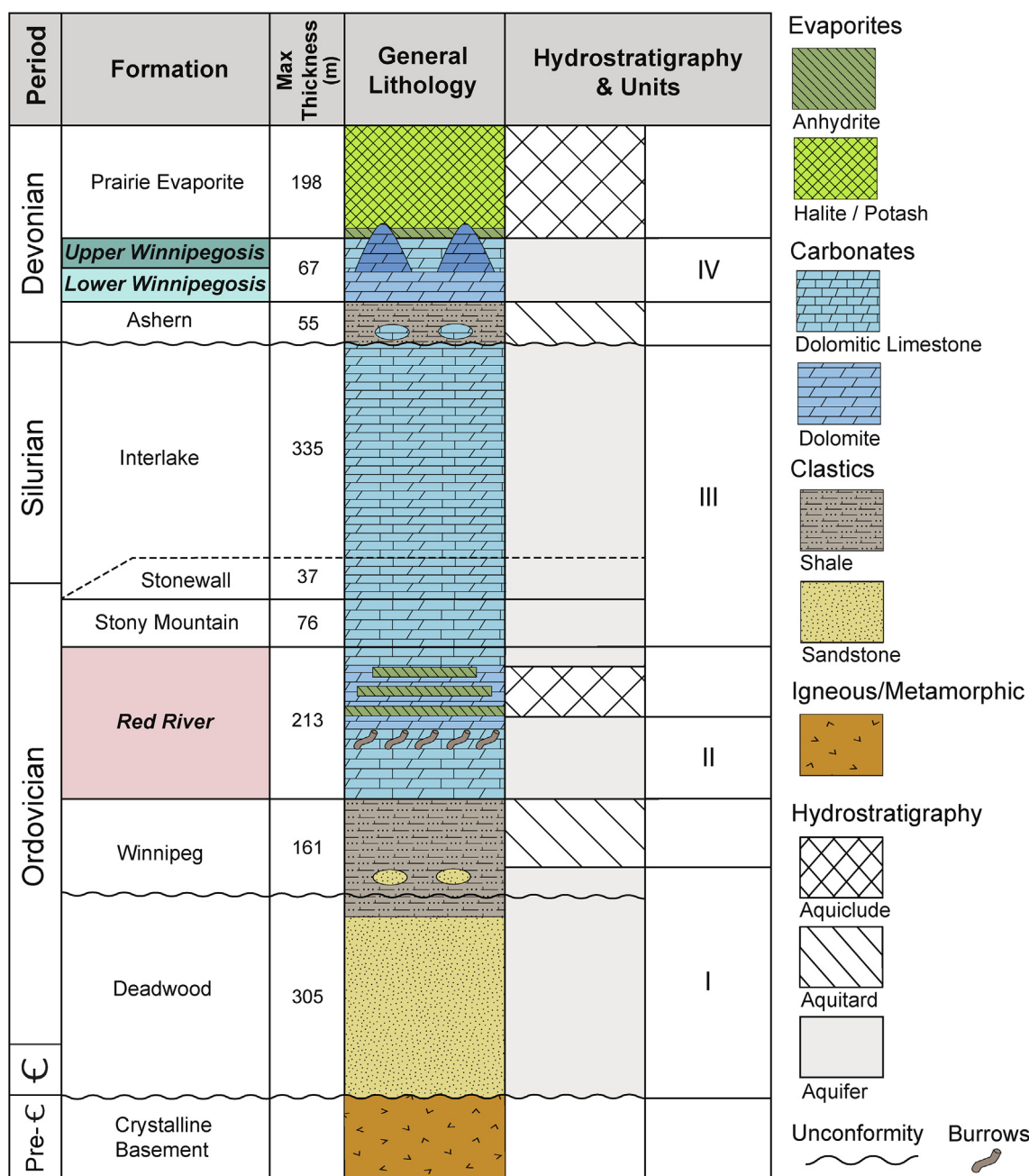


Fig. 2. Generalized stratigraphy, lithologies, and hydrostratigraphy of lower Paleozoic basal aquifer system of the Williston Basin (figure modified from [Murphy et al., 2009](#)).

matrix carbonate surrounding the burrows, and (3) minor saddle dolomite cement. As it is common to find the ‘C’ Member with dolomitized burrows and limestone matrix, the dolomitization of the burrows and matrix are considered different stages of dolomitization. All three types of dolomite record  $^{87}\text{Sr}/^{86}\text{Sr}$  ratios (0.7084–0.7097) that are higher than Late Ordovician seawater (0.7079–0.7080) ([Qing et al., 1998](#); [Holmden, 2009](#)), leading previous workers to suggest that the dolomitizing fluid may not have been evaporatively concentrated seawater filtering downward

into the carbonates from above, but rather sedimentary formation waters with high  $^{87}\text{Sr}/^{86}\text{Sr}$  ratios flowing upwards from below. Magnesium isotopes were studied in a core containing burrow, matrix, and saddle dolomite by [Worsham et al. \(2013\)](#) who found no differences in  $\delta^{26}\text{Mg}$  values among the three dolomite types at the hand sample scale. These authors concluded that if burrow, matrix, and saddle dolomite represent different stages of dolomitization, then the burrow dolomite was overprinted by younger Mg-bearing fluids that formed the matrix and sad-

dle dolomite, suggesting the possibility that the early diagenetic protodolomite may have been overprinted by interactions with Mg-bearing fluids during burial.

## 2.2. Winnipegosis Formation

The Winnipegosis Formation was deposited in a sub-basin of the Middle Devonian Elk Point Basin in Saskatchewan. The Winnipegosis directly underlies the Middle Devonian Prairie Evaporite Formation and is subdivided into Lower and Upper members. Dolomitization was partial in some areas and complete in others. The Lower Member is underlain by mixed carbonate/shale lithologies of the Ashern Formation (Lobdell, 1984). The Upper Member consists of carbonate buildups called Pinnacle Reefs, or mud mounds because they contain more mud than skeletal fragments (e.g., Reinson and Wardlaw, 1972; Gendzwill and Wilson, 1987; Fu et al., 2006). The Pinnacle Reefs formed in deeper waters in the center of the Saskatchewan sub-basin (Kendall, 1975) where they reached heights of 90 m above the seafloor with diameters of 0.5 km to 6 km (Gendzwill, 1978; Martindale et al., 1991). The Lower Member Winnipegosis is composed of 7–16 m of moderately fossiliferous wackestone (Reinson and Wardlaw, 1972; Perrin, 1982). Lithological descriptions and selected petrographic analysis of the Winnipegosis carbonates may be found in Jones (1965), Jin and Bergman (1999, 2001) and Fu et al. (2006).

Where the Elk Point Basin overlies the Williston Basin, its sedimentary strata are tilted towards the center of the Williston Basin in North Dakota. Circulation in the Elk Point Basin became restricted at the Presqu'île Barrier Reef Complex in northern Alberta in the Middle Devonian (Maiklem, 1971), turning the Saskatchewan portion of the Elk Point Basin into a hypersaline sea and eventually an evaporite basin concurrent with deposition of the Pinnacle Reefs. Gypsum and halite salts were initially deposited between the reefs, but as the basin filled with evaporites, the Pinnacle Reefs were slowly buried by impermeable salt (Fig. 2).

Fu et al. (2006) studied dolomitization of the Winnipegosis using several cores collected near the city of Saskatoon, Saskatchewan (Fig. 1b). They recognized two types of dolomite based on petrographic analysis: Type 1 in the Upper Member Winnipegosis Pinnacle Reefs, and Type 2 in the Lower Member Winnipegosis carbonate platform that supported and surrounded the reefs. The two dolomite types exhibit different crystal sizes and geochemistry. Type 1 dolomite is cryptocrystalline ( $<5\ \mu\text{m}$ ) to finely crystalline (20–60  $\mu\text{m}$ ) and records a Middle Devonian seawater  $^{87}\text{Sr}/^{86}\text{Sr}$  ratio (0.7079) (Fu et al., 2006). This finding implies dolomitization by seawater, or evaporatively concentrated seawater, filtering downward through the reefs. Type 2 dolomite is medium crystalline ( $>60\ \mu\text{m}$ ) with higher and more variable  $^{87}\text{Sr}/^{86}\text{Sr}$  ratios (0.7081–0.7093), which is inconsistent with dolomitization by seawater. This led Fu et al. (2006) to conclude that Type 2 dolomite must have formed from fluids migrating upwards from deeper in the basin where present day formation waters are known to have high  $^{87}\text{Sr}/^{86}\text{Sr}$  ratios (Rostron and Holmden, 2000).

This is the same explanation offered by Qing et al. (2001) to explain high  $^{87}\text{Sr}/^{86}\text{Sr}$  ratios in burrow, matrix, and saddle dolomite in the underlying Red River.

## 3. SAMPLING AND ANALYTICAL METHODS

### 3.1. Core sampling and elemental concentrations

Sampling was performed using a handheld drill equipped with a tungsten carbide bone crusher bit (cf., Worsham et al., 2013; Fig. S2) on cores housed by facilities in Saskatchewan, Manitoba, and North Dakota. Red River cores with 'C' Member carbonate composed of dolomitized burrows and matrix limestone were selected to avoid sampling a Mg isotopic signature in the burrow dolomite that may have been overprinted by later matrix dolomitization. Burrow dolomite and matrix limestone were sampled up to six times at the hand sample scale in each core (Table S1, Figs. S2–S3). The Winnipegosis carbonate is partially to pervasively matrix dolomitized. Each Winnipegosis core was sampled up to four times from the same core box (representing  $<1\ \text{m}$  of stratigraphic thickness) (Table S2). Sampling was focussed on the Lower Member dolomite, apart from one core (12–30–38–7W3) where four closely spaced samples were taken from dolomite in the Upper Member Pinnacle Reef (Table S2).

Powdered samples were dissolved in 50 ml centrifuge tubes using twice the stoichiometric amount of ultrapure 1.0 N HCl required for complete dissolution of the carbonate. Solutions were centrifuged after the effervescence ceased and the supernatant was decanted into acid leached Savillex<sup>TM</sup> beakers and dried. Any residue remaining after dissolution was tested with a drop of ultrapure 6 N HCl to ensure the complete digestion of all carbonate minerals. The supernatant was diluted to make a 45 ml stock solution in 0.3 N HCl. Aliquots of stock solutions were dried and redissolved in 0.3 N HNO<sub>3</sub> for Mg, Ca, Fe and Mn concentration analysis by inductively-coupled plasma optical emission spectroscopy (ICP-OES) using a SPECTRO SPECTROBLUE instrument, and inductively-coupled plasma mass spectrometry (ICP-MS) using a Perkin Elmer NexION 300D instrument, both housed in the Aqueous Geochemistry Laboratory in the Department of Geological Sciences, University of Saskatchewan (Winnipegosis samples), and high resolution ICP-MS using a Thermo Scientific ELEMENT 2 instrument in the Department of Earth and Environmental Sciences Keck Elemental Geochemistry Laboratory at the University of Michigan (Red River samples) with uncertainties typically better than  $\pm 10\%$  ( $2\sigma$ ).

### 3.2. Mg and Sr isotopes

Magnesium was purified from matrix elements prior to isotopic analysis. A two-stage traditional gravity flow column was used for the Red River samples, packed with 2 ml of Bio-Rad AG MP50 cation exchange resin, and using 1 N HCl and 1 N HNO<sub>3</sub> as the eluents. Automated ion chromatography (Thermo Scientific Dionex ICS-5000) with fraction collection was used to purify the Winnipegosis samples, equipped with an IonPac CS16  $5 \times 50\ \text{mm}$  guard

column and IonPac CS16 5 × 250 mm analytical column, which uses methanesulfonic acid as the eluent (Schmitt et al., 2009). Recovery of Mg was monitored from the gravity flow columns and the IC and confirmed to be > 95% with negligible Mg blanks (Nadeau, 2019).

Magnesium isotopes were analyzed by multiple-collector ICP-MS using a Thermo Scientific NEPTUNE instrument housed in the Saskatchewan Isotope Laboratory (SIL) in the Department of Geological Sciences, University of Saskatchewan. Solutions of Mg at 1 ppm concentrations (in 0.3 N HNO<sub>3</sub>) were introduced to the plasma by wet nebulization using a quartz double-pass cyclonic spray chamber. Ion beam intensities (8–12 V on mass 24) of the samples were matched to within 5% of the intensity of an ultrapure Mg bracketing standard (Dead Sea Magnesium - DSM3 (Galy et al., 2003), or an in-house Mg Standard (SIL-1) normalized to DSM3. Data quality was monitored using the external CAM-1 standard (Galy et al., 2003) and an internal standard made from a 1000 ppm Mg SpecPure ICP-MS standard solution. Interfering matrix elements were also checked prior to isotopic analysis to minimize the effects of molecular interferences (Galy et al., 2001).

The <sup>26</sup>Mg/<sup>24</sup>Mg ratios are reported as  $\delta^{26}\text{Mg}$  values in the conventional delta notation as *per mil* (‰) deviations of the sample isotope ratio relative to DSM3 (Eq. (2)).

$$\delta^{26}\text{Mg}_{\text{DSM3}} = \left( \frac{(^{26}\text{Mg}/^{24}\text{Mg})_{\text{sample}}}{(^{26}\text{Mg}/^{24}\text{Mg})_{\text{DSM3}}} - 1 \right) \times 1000 \quad (2)$$

The external precision of the  $\delta^{26}\text{Mg}$  values is  $\pm 0.11\text{‰}$  ( $2\sigma$ ,  $n = 140$ ), based on repeated analyses of the CAM-1 standard. North Atlantic seawater (OSIL) was measured as an additional test of our procedures, yielding  $-0.79 \pm 0.08\text{‰}$ ,  $2\sigma$   $n = 18$ , consistent with the  $\delta^{26}\text{Mg}$  value of seawater reported in the literature with a mean of  $-0.83\text{‰}$   $\pm 0.09\text{‰}$ ,  $2\sigma$   $n = 90$  (Ling et al., 2011).

Strontium was aliquoted from the Mg stock solutions and purified using a one-stage gravity flow column packed with 2 ml of Bio-Rad AG 50-X12 cation exchange resin. Strontium isotopes were measured on a thermal ionization mass spectrometer (TIMS) (Thermo Scientific TRITON) in the SIL. The <sup>87</sup>Sr/<sup>86</sup>Sr measurements were corrected for instrumental mass bias using an exponential law applied to measurements of <sup>86</sup>Sr/<sup>88</sup>Sr with an assumed true ratio of 0.1194. The external precision is estimated from repeated analyses of NIST SRM 987 yielding  $0.710262 \pm 16$  ( $2\sigma$ ).

Dolomite  $\delta^{26}\text{Mg}$  values and <sup>87</sup>Sr/<sup>86</sup>Sr ratios were plotted against their geographical coordinates on a combined map of the Elk Point and Williston basins (Fig. 3a, b). A graphical technique ( $\delta^{26}\text{Mg}$  vs. Ca/Mg) (Kimmig and Holmden, 2017) was employed to determine the end-member dolomite  $\delta^{26}\text{Mg}$  values in cores of Red River carbonate containing mixtures of burrow dolomite and matrix limestone (Fig. S2), as well as for a few Lower Member Winnipegosis cores from North Dakota that were partially dolomitized (Nadeau et al., 2019). The method of Kimmig and Holmden (2017) was also used to calculate the fractions of dolomite and calcite in the samples.

The dolomite <sup>87</sup>Sr/<sup>86</sup>Sr ratio for each core was selected from the sample with the highest dolomite abundance,

though in a few cases of partially dolomitized Winnipegosis cores a graphical technique was employed using plots of  $\delta^{26}\text{Mg}$  vs. Sr/Mg and Sr/Mg vs. <sup>87</sup>Sr/<sup>86</sup>Sr to determine the dolomite end-member <sup>87</sup>Sr/<sup>86</sup>Sr ratios (Nadeau et al., 2019).

Contour maps of dolomite  $\delta^{26}\text{Mg}$  values and <sup>87</sup>Sr/<sup>86</sup>Sr ratios were made using Surfer® 15 software with interpolation by Kriging. Inferred paleofluid flow directions are shown perpendicular to the isotopic contours.

### 3.3. Clumped Isotopes

Clumped isotope analyses were performed at the University of Miami. Samples consisted of 8–10 mg of powder split between two copper-boats loaded into a sample carousel sitting above a common acid bath containing 105% phosphoric acid (H<sub>3</sub>PO<sub>4</sub>) at 90°C that was constantly stirred using a Pyrex™ coated magnetic stir-bar. The length of reaction time was 30–60 minutes, increasing with the amount of dolomite in the sample. The extraction line is described in detail in Murray et al. (2016). The produced CO<sub>2</sub> was purified using a series of traps to remove water and a U-trap filled with Porapak™ Type Q 50–80 mesh packing material (–25 to –30°C), stored in removable sealed collection vessels and analyzed using a Thermo Scientific 253 gas source mass spectrometer.

Samples were measured against a cryogenically purified in house reference gas (RG) calibrated against NBS 19 and reported relative to VPDB ( $\delta^{13}\text{C} = -9.8\text{‰}$ ,  $\delta^{18}\text{O} = -7.4\text{‰}$ ). The extracted signal was balanced to 12 V on mass-44. The  $\delta^{13}\text{C}$  and  $\delta^{18}\text{O}$  values are produced by simultaneously measuring masses 44, 45 and 46 and correcting for the typical isobaric interferences including acid digestion fractionation on  $\delta^{18}\text{O}$  values using the fractionation factor of 1.0795 (Swart et al., 1991). In addition, the  $\delta^{18}\text{O}$  values of the samples which were >90% dolomite were corrected for the differential fractionation of dolomite relative to calcite using an additional correction factor of  $-0.8\text{‰}$  (Land, 1980).

The pressure baseline (PBL) correction, as described in He et al. (2012), was used in this study. The PBL measurements were performed with six acquisitions of fifteen on-peak click-clacks that were preceded and succeeded by five off-peak click-clacks measuring the background of the different mass voltages on the mass spectrometer. To check for long term stability in the measurements of  $\Delta_{47}$  values, an in-house Carrara marble standard was measured daily prior to any sample measurements and compared to accepted values (Dennis et al., 2011).

The raw  $\Delta_{47}$  values were calculated following the methods described by Huntington et al. (2009) using the <sup>17</sup>O correction values suggested by Brand et al. (2010), based on recommendations from within the clumped isotope community (Daëron et al., 2016; Schauer et al., 2016). These parameters have been used even though the equilibrated gases yield results that are only minimally different (<0.005‰) from those using the Brand et al. (2010) values based on Craig (1957). The raw  $\Delta_{47}$  values are converted to the carbon dioxide equilibrated scale (CDES) following the guidelines described in Dennis et al. (2011). Gas standards were created using four different CO<sub>2</sub> gases with a



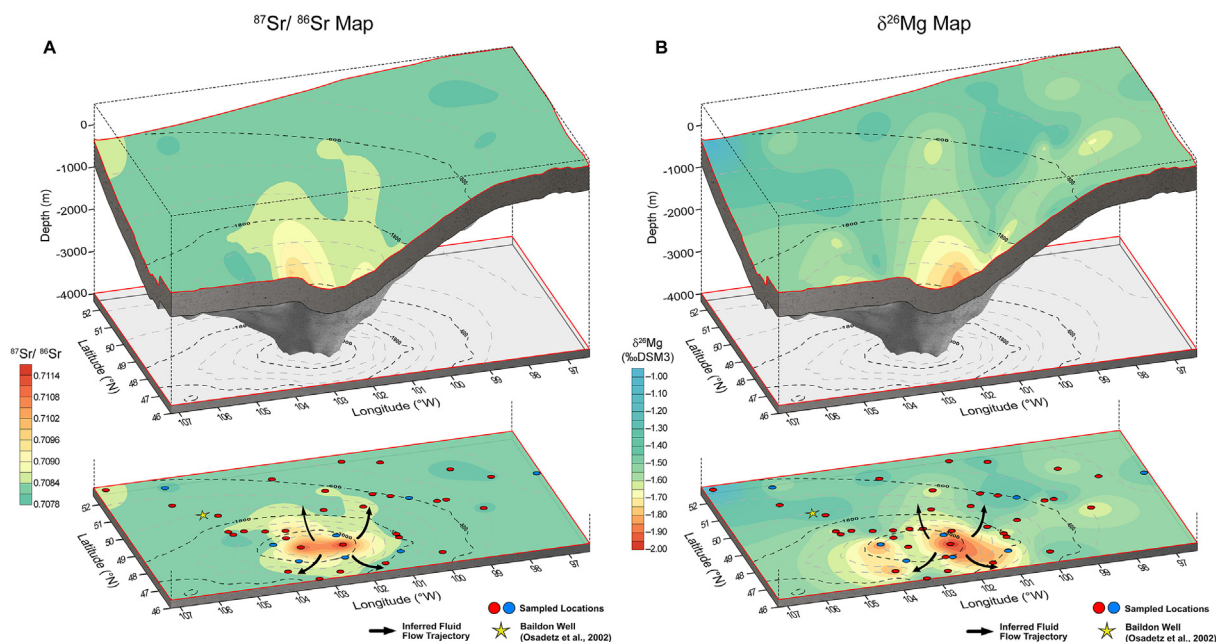


Fig. 3. Contoured 3D maps of A)  $^{87}\text{Sr}/^{86}\text{Sr}$  ratios, and B)  $\delta^{26}\text{Mg}$  values in burrow dolomite from the ‘C’ Member carbonate of the Red River and matrix dolomite from the Lower Member Winnipegosis. Fluids ascended from the structural center of the basin perpendicular to the contours (black arrows). Red circles = sample locations. Blue circles = clumped isotope thermometry. Yellow star indicates the location of the Baildon well (Osadetz et al., 2002).

range of  $\delta^{47}$  values and equilibrated either in sealed quartz tubes at 1000°C or in sealed Pyrex<sup>TM</sup> tubes over deionized water at either 25°C or 50°C. The range in  $\delta^{47}$  values in these gases is generated both by variations in  $\delta^{13}\text{C}$  and  $\delta^{18}\text{O}$  values, unlike laboratories which use a single  $\text{CO}_2$  gas which is then equilibrated with waters of varying  $\delta^{18}\text{O}$  values. The gas standards were produced and cleaned on the same vacuum line using the same methods as the carbonate samples.

An in-house calibration between  $\Delta_{47}$  values and temperatures has been used in this study, produced by reacting synthetically produced carbonates at 90°C (Swart et al., 2019) (Eq. (3)).

$$\Delta_{47} = 0.0392 \times 10^6 / T^2 + 0.158 \quad (3)$$

Fluid  $\delta^{18}\text{O}$  values were calculated using the clumped isotope temperature with Eq. (3) and the calibrations of Kim and O’Neil (1997) for calcite (Eq. (4)) and Matthews and Katz (1977) for dolomite (Eq. (5)). In these equations,  $\alpha$  is the fractionation factor between the mineral and the fluid.

$$1000 \ln \alpha = 18.03 \times 10^3 / T - 32.42 \quad (4)$$

$$1000 \ln \alpha = 3.06 \times 10^6 / T^2 - 3.24 \quad (5)$$

The Matthews and Katz (1977) equation was chosen in preference to a more recent equation by Horita (2014) as it provides more realistic values for fluids in other studies (Murray and Swart, 2017). A comprehensive analysis of the ETH standards analyzed from 2018–2019 are included in Swart et al. (2019).

#### 4. RESULTS

Maps of dolomite  $^{87}\text{Sr}/^{86}\text{Sr}$  ratios (Fig. 3a) and  $\delta^{26}\text{Mg}$  values (Fig. 3b) are constructed using data from both dolomite bodies (Tables 1; S1, S2). Individual maps can be viewed in the *Supplementary Materials* (Figs. S4, S5). Combining the respective data into two maps is justified by the spatially similar ranges in the isotopic values. All maps show radially concentric patterns of decreasing  $^{87}\text{Sr}/^{86}\text{Sr}$  ratios ( $\sim 0.710$  to  $0.708$ ) and increasing  $\delta^{26}\text{Mg}$  values ( $\sim -2.0\text{‰}$  to  $-0.96\text{‰}$ ) from the center to the edges of the Williston Basin.

Six Red River and two Winnipegosis cores were targeted for carbonate clumped isotope thermometry with 2–6 measurements performed at the hand sample scale in the Red River cores, and 2–4 measurements at the core box scale in the Winnipegosis cores. Burrow dolomite temperatures in the Red River cores are higher in the center of the Williston Basin ( $92 \pm 9^\circ\text{C}$ ) than along the edges ( $45 \pm 14^\circ\text{C}$ ,  $n = 4$ ,  $1\sigma$ ) (Fig. 4e; S2) (Tables 2, S3). Matrix calcite gave similar temperatures to the burrow dolomite in most of the cores, with the exception of ND 8553 at mid-basin depth (2.4 km) which gave  $70 \pm 9^\circ\text{C}$  ( $1\sigma$ ) for burrow dolomite and  $44 \pm 1^\circ\text{C}$  ( $1\sigma$ ) for matrix calcite (Table 2). Temperatures correlate with dolomite abundance in the burrows of the deepest Red River core (ND 7362; Table S3) and both Winnipegosis cores.

Mixtures of two carbonate phases (e.g., dolomite and calcite) with different  $\Delta_{47}$  values imply mixed temperatures or mixed apparent temperatures. Mixing is linear if  $\delta^{13}\text{C}$  and  $\delta^{18}\text{O}$  values of the dolomite and calcite end-members



Table 1  
Sr and Mg isotope end-member data for Red River and Winnipegosis dolomites.

| Core ID              | State/Province | Well Location    | Northing | Westing  | Depth (m) | $^{87}\text{Sr}/^{86}\text{Sr}$ | $\delta^{26}\text{Mg}$<br>DSM3 |
|----------------------|----------------|------------------|----------|----------|-----------|---------------------------------|--------------------------------|
| <b>RED RIVER</b>     |                |                  |          |          |           |                                 |                                |
| Tyndall Stone        | MB             | Garson Quarry    | 50.103   | −96.609  | Outcrop   | 0.708144                        | −1.46                          |
| MB 1660              | ND             | 04-06-015-02W1   | 50.243   | −97.734  | 187       | 0.708077                        | −1.52                          |
| ND 31                | ND             | NWSW 32-160-60   | 48.638   | −98.416  | 714       | 0.708036                        | −1.67                          |
| Dome Pelican Lake    | MB             | 07-34-04-15WPM   | 49.346   | −99.396  | 1002      | 0.708177                        | −1.64                          |
| Dome Brandon         | MB             | 03-05-09-19WPM   | 49.711   | −100.003 | 1020      | 0.708270                        | −1.31                          |
| Dome Arrow River     | MB             | 12-10-14-25WPM   | 50.175   | −100.801 | 1223      | 0.708326                        | −1.45                          |
| ND 7146              | ND             | NWNE 15-136-75   | 46.602   | −100.092 | 1421      | 0.708278                        | −1.44                          |
| ND 8803              | ND             | NENE 22-151-80   | 47.890   | −100.888 | 2399      | 0.708057                        | −1.69                          |
| ND 8553              | ND             | SENE 17-140-82   | 46.944   | −101.063 | 2421      | 0.708260                        | −1.77                          |
| ND 8549              | ND             | SESE 16-134-87   | 46.417   | −101.614 | 2530      | 0.708200                        | −1.80                          |
| CPG Minton           | SK             | 03-17-03-21W-2 M | 49.205   | −104.801 | 2811      | 0.708445                        | −1.65                          |
| ND 14491             | ND             | NWNE 27-130-102  | 46.061   | −103.419 | 2902      | 0.708295                        | −1.44                          |
| Imperial Hummingbird | SK             | 06-13-02-19W2    | 49.122   | −104.424 | 3031      | 0.708463                        | −1.55                          |
| ND 8010              | ND             | NWNE 25-133-97   | 46.303   | −102.810 | 3129      | 0.708597                        | −1.62                          |
| ND 10624             | ND             | NESE 9-163-102   | 48.958   | −103.928 | 3223      | 0.708319                        | −1.42                          |
| ND 6272              | ND             | LT2 22-137-106   | 46.670   | −104.041 | 3245      | 0.708426                        | −1.83                          |
| ND 8088              | ND             | NWNE 28-141-93   | 47.008   | −102.470 | 3587      | 0.708675                        | −1.89                          |
| ND 9033              | ND             | NESW 4-142-102   | 47.142   | −103.619 | 3832      | 0.708832                        | −1.65                          |
| ND 7362              | ND             | NESW 13-155-91   | 48.246   | −102.323 | 3948      | 0.708535                        | −1.80                          |
| ND 10893             | ND             | CNE 1-157-100    | 48.453   | −103.548 | 4029      | 0.708843                        | −1.54                          |
| ND 7631              | ND             | NENE 33-151-99   | 47.861   | −103.350 | 4289      | 0.708945                        | −1.59                          |
| <b>WINNIPEGOSIS</b>  |                |                  |          |          |           |                                 |                                |
| 13-30-022-08W1       | MB             | 13-30-022-08W1   | 50.931   | −98.572  | 24        | 0.707986                        | −1.60                          |
| 1-05-033-19W1        | MB             | 1-05-033-19W1    | 51.799   | −100.109 | 132       | 0.708144                        | −1.43                          |
| 3-29-036-25W1        | MB             | 3-29-036-25W1    | 52.115   | −101.003 | 244       | 0.708152                        | −1.45                          |
| 16-33-004-13W1       | MB             | 16-33-004-13W1   | 49.353   | −99.159  | 680       | 0.708282                        | −1.35                          |
| 4-27-011-22W1        | MB             | 4-27-011-22W1    | 49.948   | −100.413 | 863       | 0.708097                        | −1.34                          |
| 4-27-31-7W2          | SK             | 4-27-31-7W2      | 51.680   | −102.925 | 931       | 0.708237                        | −1.41                          |
| 1-04-020-32W1        | SK             | 1-04-020-32W1    | 50.683   | −101.861 | 1085      | 0.708447                        | −1.64                          |
| 1-12-035-26W2        | SK             | 1-12-035-26W2    | 51.986   | −105.578 | 1119      | 0.707999                        | −1.53                          |
| 12-30-38-7W3         | SK             | 12-30-38-7W3     | 52.299   | −107.000 | 1081–1166 | 0.708614                        | −0.96                          |
| 02-21-007-28W1       | MB             | 02-21-007-28W1   | 49.579   | −101.222 | 1447      | 0.708568                        | −1.50                          |
| 16-158-75            | ND             | 16-158-75        | 48.400   | −102.068 | 1466      | —                               | −1.82                          |
| 10-34-23-27-W2       | SK             | 10-34-23-27-W2   | 51.003   | −105.691 | 1568      | 0.708311                        | −1.43                          |
| 04-02-014-21W2       | SK             | 04-02-014-21W2   | 50.136   | −104.779 | 1883      | 0.708084                        | −1.36                          |
| 13-27-008-2W2        | SK             | 13-27-008-2W2    | 49.681   | −102.207 | 1907      | 0.708207                        | −1.60                          |
| 2-156-82             | ND             | 2-156-82         | 48.362   | −101.168 | 2115      | —                               | −1.47                          |
| 26-149-80            | ND             | 26-149-80        | 47.691   | −100.877 | 2138      | 0.708390                        | −1.56                          |
| 2-10-1-21W2          | SK             | 2-10-1-21W2      | 49.015   | −104.730 | 2733      | 0.707880                        | −1.51                          |
| 29-157-88            | ND             | 29-157-88        | 48.503   | −100.361 | 3070      | —                               | −1.56                          |
| 20-162-98            | ND             | 20-162-98        | 48.848   | −103.439 | 3100      | 0.709721                        | −1.59                          |
| 5-161-95             | ND             | 5-161-95         | 48.806   | −103.029 | 3135      | —                               | −1.64                          |
| 4-160-93             | ND             | 4-160-93         | 48.717   | −102.711 | 3326      | —                               | −1.71                          |
| 6-141-94             | ND             | 6-141-94         | 47.063   | −102.633 | 3408      | —                               | −1.65                          |
| 22-149-91            | ND             | 22-149-91        | 47.712   | −102.313 | 3520      | 0.711724                        | −2.02                          |
| 5-154-103            | ND             | 5-154-103        | 48.192   | −103.957 | 3637      | 0.708236                        | −1.89                          |

differ by less than a few *per mil* (Defliese and Lohmann, 2015; Murray et al., 2020), which is the case in this study (Table 2). However, most of the temperatures do not improve in quality or reliability with unmixing, either because the sampling of the core successfully targeted predominantly burrow dolomite and matrix calcite, or the difference in end-member  $\Delta_{47}$  values is small compared to the measurement uncertainties, thus resulting in poor regression statistics. Graphs of three cores with unmixed temperatures can be found in the *Supplementary Materials* and

include: (1) Red River ND 7362, which shows a strong correlation between dolomite abundance and temperature, yielding  $92 \pm 9^\circ\text{C}$  for the end-member burrow dolomite; (2) Winnipegosis core 5–154-103, yielding  $219 \pm 91^\circ\text{C}$  ( $n = 4$ , 1se) for end-member matrix dolomite with a large temperature uncertainty; and (3) Winnipegosis core 07–02-038–01W3, yielding  $103^\circ\text{C}$  for end-member matrix dolomite using a two-point regression (Table S3).

Dolomite paleotemperatures are combined with dolomite  $\delta^{18}\text{O}$  values to calculate the  $\delta^{18}\text{O}$  values of the waters

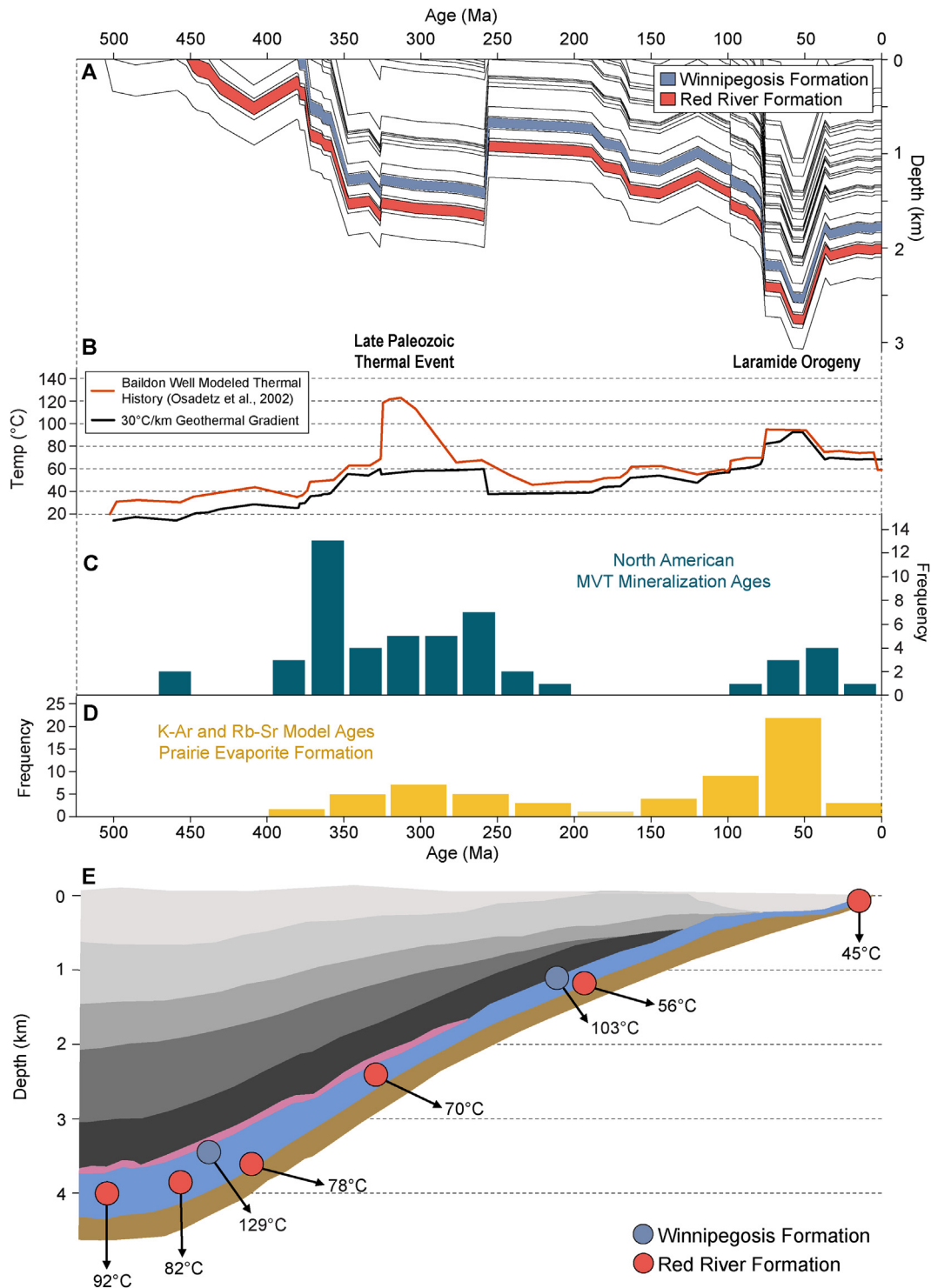


Fig. 4. A) Burial history model of the Baildon well (02-011-15-26W2 or 50.239°N 105.474°W) modified from Osadetz et al. (2002). B) Modeled basement (Deadwood Formation) temperature history (orange line) of the Baildon well showing Late Devonian / Early Carboniferous heat flow anomaly (modified from Osadetz et al., 2002). Temperature history (black line) based on stratigraphic constraints (geothermal gradient of 30°C/km). C) Frequency histogram for MVT mineralization in North America (Leach et al., 2001; Taylor et al., 2009, and references therein). D) Frequency histogram for K/Ar-Rb/Sr dating of Prairie Evaporite Formation minerals. Figure modified from Koehler et al. (1997). E) Clumped isotope thermometry of samples located within the Winnipegosis (blue) and underlying Red River (red) Formations taken from either the average values of dolomite from each formation, or unmixed temperature end members (Table 2), depicting the sampling depth and relative location in the Williston Basin as it exists today.

Table 2

Clumped isotope paleotemperatures and supportive data for selected carbonate samples from the Red River and Winnipegosis.

| Core and sample names                | Type       | Depth<br>(m) | $^{87}\text{Sr}/^{86}\text{Sr}$ | $\delta^{26}\text{Mg}$<br>DSM3 | Mg/Ca<br>(mol) | Dolomite <sup>1</sup><br>(mol%) | $\delta^{13}\text{C}$<br>VPDB | $\delta^{18}\text{O}_{\text{carb}}$<br>VPDB | $\Delta_{47}^3$<br>(‰) | Temp<br>(°C)     | $\delta^{18}\text{O}_{\text{fluid}}^4$<br>VSMOW |
|--------------------------------------|------------|--------------|---------------------------------|--------------------------------|----------------|---------------------------------|-------------------------------|---|------------------------|------------------|---|
| <b>Tyndall Stone (Red River)</b>     |            |              |                                 |                                |                |                                 |                               |   |                        |                  |   |
| 50.103N, 96.609W                     |            |              |                                 |                                |                |                                 |                               |   |                        |                  |   |
| GQTS 2                               | Matrix     | Outcrop      | 0.70797                         | −2.16                          | 0.01           | 1.2                             | −1.11                         | −7.91                                       | 0.53                   | 50               | −0.9  |
| GQTS 4                               | Matrix     | Outcrop      | 0.70798                         | −2.10                          | 0.02           | 1.4                             | −1.02                         | −7.80                                       | 0.50                   | 66               | 1.8   |
| GQTS 6                               | Matrix     | Outcrop      | 0.70797                         | −1.98                          | 0.02           | 2.3                             | −1.10                         | −7.75                                       | 0.58 ± 0.02            | 33 ± 9           | −3.8 ± 1.7                                      |
|                                      |            |              |                                 |                                |                |                                 |                               |   |                        | avg              | 50 ± 16   |
|                                      |            |              |                                 |                                |                |                                 |                               |   |                        | avg              | −1 ± 3  |
| GQTS 1                               | Burrow     | Outcrop      | 0.70818                         | −1.52                          | 0.82           | 90                              | −0.04                         | −6.95                                       | 0.58                   | 31               | −7.1  |
| GQTS 3                               | Burrow     | Outcrop      | 0.70813                         | −1.48                          | 0.79           | 88                              | −0.17                         | −6.98                                       | 0.55                   | 45               | −4.3  |
| GQTS 5                               | Burrow     | Outcrop      | 0.70814                         | −1.37                          | 0.89           | 94                              | −0.09                         | −6.70                                       | 0.51                   | 59               | −1.6  |
| Mixing end-members                   |            |              |                                 |                                |                |                                 |                               |   |                        | avg              | 45 ± 14   |
|                                      |            |              |                                 |                                |                |                                 |                               |   |                        | avg              | −4.3 ± 2.7                                      |
| Dolomite                             | Burrow     |              |                                 | −1.46                          | 1.00           |                                 | −0.03                         | −6.80                                       |                        |                  |   |
| Limestone                            | Matrix     |              |                                 | −2.19                          | 0.01           |                                 | −1.20                         | −7.95                                       |                        |                  |   |
| <b>Dome Brandon (Red River)</b>      |            |              |                                 |                                |                |                                 |                               |   |                        |                  |   |
| 49.711N, 100.003W                    |            |              |                                 |                                |                |                                 |                               |   |                        |                  |   |
| 1                                    | Matrix     | 1020         | -                               | −1.71                          | 0.03           | 4.3                             | −0.40                         | −7.17                                       | 0.54 ± 0.04            | 48 ± 15          | −0.5 ± 2.5                                      |
| 2                                    | Matrix     | 1020         | -                               | −1.40                          | 0.12           | 19                              | −0.47                         | −6.95                                       | 0.51                   | 62               | 2.1   |
| 3                                    | Matrix     | 1020         | 0.70812                         | −1.80                          | 0.03           | 3.3                             | −0.51                         | −7.35                                       | 0.52 ± 0.01            | 59 ± 4           | 0.6 ± 0.7                                       |
|                                      |            |              |                                 |                                |                |                                 |                               |   |                        | avg              | 56 ± 7  |
|                                      |            |              |                                 |                                |                |                                 |                               |   |                        | avg              | 0.7 ± 1.3                                       |
| 4                                    | Burrow     | 1020         | 0.70827                         | −1.30                          | 0.50           | 66                              | 0.20                          | −4.35                                       | 0.51                   | 62               | 1.1   |
| 5                                    | Burrow     | 1020         | -                               | −1.34                          | 0.51           | 66                              | 0.30                          | −4.34                                       | 0.53 ± 0.05            | 52 ± 22          | −0.6 ± 4.0                                      |
| 6                                    | Burrow     | 1020         | -                               | −1.35                          | 0.42           | 58                              | 0.15                          | −4.73                                       | 0.52                   | 55               | −0.3  |
| Mixing end-members                   |            |              |                                 |                                |                |                                 |                               |   |                        | avg              | 56 ± 5  |
|                                      |            |              |                                 |                                |                |                                 |                               |   |                        | avg              | −0.8 ± 0.9                                      |
| Dolomite                             | Burrow     |              |                                 | −1.31                          | 1.00           |                                 | 0.60                          | −2.50                                       |                        |                  |   |
| Limestone                            | Matrix     |              |                                 | −1.81                          | 0.03           |                                 | −0.50                         | −7.50                                       |                        |                  |   |
| <b>07–02-038–01W3 (Winnipegosis)</b> |            |              |                                 |                                |                |                                 |                               |   |                        |                  |   |
| 52.237N, 106.037W                    |            |              |                                 |                                |                |                                 |                               |   |                        |                  |   |
| 1                                    | Whole Rock | 1188         | -                               | -                              | -              | 47                              | 1.19                          | −5.89                                       | 0.48 ± 0.02            | 79 ± 11          | 2.2 ± 1.4                                       |
| 2                                    | Whole Rock | 1188         | -                               | -                              | -              | 1.1                             | 3.51                          | −5.60                                       | 0.52 ± 0.04            | 58 ± 16          | 2.7 ± 2.6                                       |
| Mixing end-members                   |            |              |                                 |                                |                |                                 |                               |   |                        | avg              | 68 ± 15   |
|                                      |            |              |                                 |                                |                |                                 |                               |   |                        | avg              | 2.5 ± 0.4                                       |
| Dolomite                             | end-member |              |                                 |                                |                |                                 |                               |   |                        | 103 <sup>5</sup> |   |
| Limestone                            | end-member |              |                                 |                                |                |                                 |                               |   |                        | 57               |   |
| <b>ND 8553 (Red River)</b>           |            |              |                                 |                                |                |                                 |                               |   |                        |                  |   |
| 46.944N, 101.063W                    |            |              |                                 |                                |                |                                 |                               |   |                        |                  |   |
| 1                                    | Matrix     | 2421         | -                               | −1.86                          | 0.06           | 10                              | -                             | -   | -                      | -                | -   |
| 2                                    | Matrix     | 2421         | -                               | −2.06                          | 0.04           | 6.8                             | 0.59                          | −5.89                                       | 0.55                   | 44               | 1.2   |
| 3                                    | Matrix     | 2421         | 0.70798                         | −2.35                          | 0.02           | 3.1                             | 0.52                          | −5.93                                       | 0.55                   | 45               | 4.1   |

|                                 |            |      |         |       |      |     |       |       |             |     |                       |     |           |
|---------------------------------|------------|------|---------|-------|------|-----|-------|-------|-------------|-----|-----------------------|-----|-----------|
| 4                               | Burrow     | 2421 | -       | -1.86 | 0.68 | 80  | 1.39  | -5.41 | 0.51        | avg | 44 ± 1                | avg | 2.7 ± 2.1 |
| 5                               | Burrow     | 2421 | -       | -1.84 | 0.38 | 54  | -     | -     | -           |     | 63                    |     | 0.4       |
| 6                               | Burrow     | 2421 | 0.70826 | -1.75 | 0.75 | 85  | 1.43  | -4.51 | 0.48        |     | 76                    |     | 3.3       |
| Mixing end-members              |            |      |         |       |      |     |       |       |             | avg | 70 ± 9                | avg | 1.9 ± 2.1 |
| Dolomite                        | Burrow     |      |         | -1.77 | 1.00 |     | 1.60  | -4.31 |             |     |                       |     |           |
| Limestone                       | Matrix     |      |         | -2.30 | 0.03 |     | 0.50  | -5.95 |             |     |                       |     |           |
| <b>ND 8088 (Red River)</b>      |            |      |         |       |      |     |       |       |             |     |                       |     |           |
| 47.008N, 102.470W               |            |      |         |       |      |     |       |       |             |     |                       |     |           |
| 1                               | Matrix     | 3587 | -       | -2.12 | 0.08 | 13  | -     | -     | -           |     | -                     |     | -         |
| 2                               | Matrix     | 3587 | -       | -2.76 | 0.02 | 2.4 | -     | -     | -           |     | -                     |     | -         |
| 3                               | Matrix     | 3587 | 0.70790 | -2.84 | 0.02 | 1.9 | -     | -     | -           |     | -                     |     | -         |
| 4                               | Burrow     | 3587 | -       | -1.90 | 0.68 | 81  | 0.66  | -5.96 | 0.46        |     | 81                    |     | 2.5       |
| 5                               | Burrow     | 3587 | -       | -1.88 | 0.33 | 49  | 0.98  | -5.58 | 0.47        |     | 87                    |     | 3.7       |
| 6                               | Burrow     | 3587 | 0.70868 | -1.90 | 0.75 | 85  | 1.09  | -5.18 | 0.50        |     | 66                    |     | 1.0       |
| Mixing end-members              |            |      |         |       |      |     |       |       |             | avg | 78 ± 11               | avg | 2.4 ± 1.3 |
| Dolomite                        | Burrow     |      |         | -1.89 | 1.00 |     | 1.22  | -5.00 |             |     |                       |     |           |
| Limestone                       | Matrix     |      |         | -2.60 | 0.03 |     | 0.35  | -6.60 |             |     |                       |     |           |
| <b>5–154-103 (Winnipegosis)</b> |            |      |         |       |      |     |       |       |             |     |                       |     |           |
| 48.192N, 103.957W               |            |      |         |       |      |     |       |       |             |     |                       |     |           |
| 1                               | Whole Rock | 3637 | 0.70809 | -1.91 | 0.25 | 39  | 1.79  | -6.60 | 0.39        |     | 142                   |     | 8.5       |
| 2                               | Whole Rock | 3637 | 0.70812 | -     | -    | 18  | 2.10  | -6.78 | 0.42        |     | 112                   |     | 5.5       |
| 3                               | Whole Rock | 3637 | 0.70825 | -1.86 | 0.21 | 34  | 1.69  | -6.84 | 0.41 ± 0.03 |     | 122 ± 25              |     | 6.3 ± 2.4 |
| 4                               | Whole Rock | 3637 | 0.70819 | -1.89 | 0.20 | 32  | 1.49  | -6.75 | 0.39 ± 0.01 |     | 141 ± 13              |     | 8.3 ± 1.1 |
| Mixing end-members              |            |      |         |       |      |     |       |       |             | avg | 129 ± 15              | avg | 7.1 ± 1.5 |
| Dolomite                        | end-member |      |         | -1.89 | 1.00 |     | 3.00  | -5.60 |             |     | 219 ± 91 <sup>5</sup> |     |           |
| Limestone                       | end-member |      |         | -2.20 | 0.03 |     | 1.40  | -7.10 |             |     | 89 ± 22               |     |           |
| <b>ND 9033 (Red River)</b>      |            |      |         |       |      |     |       |       |             |     |                       |     |           |
| 47.142N, 103.619W               |            |      |         |       |      |     |       |       |             |     |                       |     |           |
| 1                               | Matrix     | 3832 | 0.70809 | -1.78 | 0.10 | 16  | 0.26  | -6.39 | 0.47        |     | 85                    |     | 6.1       |
| 2                               | Matrix     | 3832 | -       | -2.01 | 0.04 | 5.7 | -0.17 | -6.86 | 0.45        |     | 92                    |     | 6.6       |
|                                 |            |      |         |       |      |     |       |       |             | avg | 88 ± 5                | avg | 6.3 ± 0.4 |
| 3                               | Burrow     | 3832 | 0.70883 | -1.66 | 0.84 | 91  | -     | -     | -           |     | -                     |     | -         |
| 4                               | Burrow     | 3832 | -       | -1.65 | 0.82 | 90  | 0.79  | -5.53 | 0.47        |     | 82                    |     | 3.1       |
| Mixing end-members              |            |      |         |       |      |     |       |       |             |     |                       |     |           |
| Dolomite                        | Burrow     |      |         | -1.65 | 1.00 |     | 0.87  | -5.44 |             |     |                       |     |           |
| Limestone                       | Matrix     |      |         | -3.77 | 0.01 |     | -0.16 | -6.90 |             |     |                       |     |           |



**ND 7362 (Red River)**  
48.246N, 102.323W

|                           |   |      |         |       |      |    |      |       |             |                     |            |
|---------------------------|---|------|---------|-------|------|----|------|-------|-------------|---------------------|------------|
| 1                         | Matrix  | 3948 | -       | -1.91 | 0.14 | 24 | 0.26 | -6.04 | 0.51 ± 0.05 | 64                  | -3.2 ± 3.9 |
| 2                         | Matrix  | 3948 | -       | -1.85 | 0.36 | 52 | 0.57 | -5.85 | 0.47        | 81                  | 6.1        |
| 3                         | Matrix  | 3948 | 0.70794 | -2.02 | 0.08 | 14 | 0.14 | -6.27 | 0.46        | 90                  | 6.9        |
| 4                         | Burrow  | 3948 | -       | -1.80 | 0.57 | 72 | 0.75 | -5.30 | 0.46        | avg                 | 5.4 ± 2.0  |
| 5                         | Burrow  | 3948 | 0.70854 | -1.75 | 0.74 | 85 | 0.88 | -5.38 | 0.47        | 86                  | 3.9        |
| 6                         | Burrow  | 3948 | -       | -1.90 | 0.32 | 48 | 0.48 | -5.90 | 0.50        | 82                  | 3.2        |
|                           |   |      |         |       |      |    |      |       |             | 68                  | 0.6        |
|                           |   |      |         |       |      |    |      |       |             | avg                 | 2.6 ± 1.7  |
| <b>Mixing end-members</b> |   |      |         |       |      |    |      |       |             |                     |            |
|                           | Dolomite                                      |      |         | -1.79 | 1.00 |    | 1.04 | -5.10 |             | 92 ± 9 <sup>5</sup> |            |
|                           | Limestone                                     |      |         | -2.64 | 0.03 |    | 0.05 | -6.40 |             | 57 ± 8              |            |
|                           | <i>Median basin center Red River dolomite</i> |      |         |       |      |    |      |       |             |                     | n = 7      |

1. Calculated using Mg/Ca ratios assuming dolomite has a Mg/Ca = 1.0 and a linear mixing approximation.
2. 1σ error for two or more repeated analyses of the same sample.
3. Digested at 90°C.
4. Calculated using clumped isotope temps and calibrations of Kim and O'Neil (1997) for calcite and Matthews and Katz (1977) for dolomite.
5. Winnipegosis and ND 7362 Burrow dolomite end-member temperature calculated with mixing analysis as shown in Table S3.

that formed in equilibrium with dolomite using the equation of Matthews and Katz (1977) (Eq. (5)), yielding -7.1‰ to +6.9‰ (VSMOW) for the Red River burrow dolomite, and +2.2‰ to +8.5‰ (VSMOW) for the Winnipegosis matrix dolomite. The highest  $\delta^{18}\text{O}$  values were obtained for the deepest samples and are higher than modern seawater, which is typical of evaporatively concentrated seawater (Knauth and Beeunas, 1986) and deep formation waters (Clayton et al., 1966). The formation water in equilibrium with the deepest burrow dolomite in the Red River is  $+2.6 \pm 1.7\text{‰}$  (1σ) (T = 92°C), and the deepest matrix dolomite in the Winnipegosis is  $+7.1\text{‰} \pm 1.5\text{‰}$  1σ (T = 129°C) (Table 2).

## 5. DISCUSSION

### 5.1. $^{87}\text{Sr}/^{86}\text{Sr}$ map

Field studies show that Sr concentrations are generally lower in dolomite (Vahrenkamp and Swart, 1990) than in calcite (Baker et al., 1982) formed in open systems, and two to three orders of magnitude lower than aragonite (Kinsman, 1969). This implies that during the replacement of calcite and aragonite by dolomite, dolomitizing fluids will become progressively enriched in Sr (and Ca) in the direction of fluid flow. Because the released Sr is marine in origin, the  $^{87}\text{Sr}/^{86}\text{Sr}$  ratio of the dolomitizing fluid shifts gradually towards the  $^{87}\text{Sr}/^{86}\text{Sr}$  ratio of seawater preserved in the carbonates in the direction of fluid flow. Seawater had nearly the same  $^{87}\text{Sr}/^{86}\text{Sr}$  ratio of  $\sim 0.70795 \pm 0.00005$  in both the Late Ordovician and Middle Devonian (Qing et al., 1998; Fu et al., 2006; Holmden, 2009). The isotopic map shows  $^{87}\text{Sr}/^{86}\text{Sr}$  ratios decreasing from the center to the edges of the Williston Basin in all directions ( $\sim 0.710$  to  $0.7079$ ) (Fig. 3a). Combined with the gradient in dolomite  $\delta^{26}\text{Mg}$  values (see Section 5.2), these findings are consistent with the formation of new dolomite, or the alteration of early diagenetic protodolomite, by  $^{87}\text{Sr}$  and Mg-enriched fluids ascending from the deep center of the basin. High present-day  $^{87}\text{Sr}/^{86}\text{Sr}$  ratios ( $>0.710$ ) in deep formation waters in the Williston Basin support this interpretation (Table 3) (Rostron and Holmden, 2000).

### 5.2. $\delta^{26}\text{Mg}$ map

#### 5.2.1. Rayleigh fractionation effects

Dolomite preferentially sequesters  $^{24}\text{Mg}$  when it forms. Therefore, dolomite  $\delta^{26}\text{Mg}$  values may be expected to increase in the direction of fluid flow under some conditions due to Rayleigh fractionation of the reactive Mg source. Dolomite  $\delta^{26}\text{Mg}$  values increase away from the deep center of the Williston Basin. If the Rayleigh distillation model is correct (Fig. 3b), then Mg-bearing fluids must have ascended through the Red River and Lower Member Winnipegosis carbonates. This is also the direction of fluid flow implied by the gradient in  $^{87}\text{Sr}/^{86}\text{Sr}$  ratios (Fig. 3a), lending support to the ascending fluid flow hypothesis. However, the length-scale of the  $\delta^{26}\text{Mg}$  gradient warrants caution regarding the plausibility of its origin by Rayleigh distillation (Nadeau et al., 2019). Considering the *per mil* level

Table 3

Sr isotope data and Ca and Mg concentrations for present day Deadwood, Winnipeg, and Red River “C member” formation waters.

| Well Name      | Formation   | Northing | Westing  | $^{87}\text{Sr}/^{86}\text{Sr}$ | SE       | Ca (ppm) | Mg (ppm) |
|----------------|-------------|----------|----------|---------------------------------|----------|----------|----------|
| Mott #32X-3    | Deadwood    | 48.977   | −101.939 | 0.721181                        | 0.000008 | 31400    | 2140     |
| Larson #23X-9  | Deadwood    | 48.957   | −101.969 | 0.721835                        | 0.000010 | 35300    | 2160     |
| Berkley et al. | Winnipeg    |          |          | 0.714804                        | 0.000008 | 8450     | 908      |
| Berkley et al. | Winnipeg    | 49.490   | −103.443 | 0.715240                        | 0.000007 | 10900    | 1030     |
| Drawbond 9 #3  | Red River C | 48.958   | −103.928 | 0.708688                        | 0.000012 | 34200    | 3510     |
| EIDE #35-11R   | Red River C | 47.680   | −103.318 | 0.708998                        | 0.000010 | 36100    | 2200     |

magnitude of the fractionation factor (−1.8‰ to −1.1‰ at 20°C and 100°C, respectively) (Li et al., 2015), dolomitization would have to have been very inefficient to create such a small gradient over such large distances. Moreover, the distillation of Mg isotopes should coincide with decreasing dolomite abundance in the direction of fluid flow, which is not observed.

Reactive transport simulations show that dolomite concentration decreases in the direction of fluid flow only in the reaction front region in fluid-buffered diagenetic systems (Whitaker and Xiao, 2010; Yapparova et al., 2017). Although the authors did not model Mg isotopes, we expect the fully dolomitized carbonate behind the reaction front to be uniform in isotopic composition. The basis of this prediction is the assumption that protodolomite continuously exchanges Mg with the migrating fluid until the reaction front passes and the carbonate is completely replaced. Under these conditions, the fully dolomitized carbonate inherits the  $\delta^{26}\text{Mg}$  value of the reactive Mg source, offset by the temperature dependent fractionation factor (Eq. (6)),

$$\Delta^{26}\text{Mg}_{\text{dolo-aq}} = -0.1554(\pm 0.0096) \times 10^6/T^2 \quad (6)$$

where  $\Delta^{26}\text{Mg}_{\text{dolo-aq}}$  is the fractionation factor in *per mil* ( $\equiv 1000\ln(\alpha)$ ) and  $T$  is the temperature in Kelvin (Li et al., 2015). Dolomites formed in this way will preserve gradients in  $\delta^{26}\text{Mg}$  values only near their margins where the Mg-bearing fluids lose their capacity to dolomitize. This model of fluid buffered replacement dolomitization cannot explain basin wide gradients in dolomite  $\delta^{26}\text{Mg}$  values on the scale of the Williston Basin.

### 5.2.2. Temperature effects

A gradient in dolomite  $\delta^{26}\text{Mg}$  values could be produced if fluid temperature changed along the flow path while the dolomite was forming. However, the temperature would have to increase upwards in the basin to produce the observed result, which is inconsistent with the Earth's geothermal gradient.

### 5.2.3. Physical mixing

Mixing between two types (or generations) of dolomite can produce  $\delta^{26}\text{Mg}$  gradients in dolomite bodies if the mixing is geographically controlled. Fu et al. (2006) recognized two types of dolomite in the Winnipegosis that they dubbed Type 1 and Type 2 (Section 2.2). Type 1 dolomite only occurs in the Upper Member Pinnacle Reefs. The  $^{87}\text{Sr}/^{86}\text{Sr}$  ratio of Type 1 dolomite is consistent with dolomitization by evaporatively concentrated Middle Devonian seawater

descending into the reefs from above. Type 2 dolomite with its higher  $^{87}\text{Sr}/^{86}\text{Sr}$  ratios, elevated Fe and Mn concentrations, and coarser crystal size supports dolomitization of the underlying Lower Member Winnipegosis by fluids ascending from below. Petrographic analysis shows physical mixing of the two dolomite types in a Pinnacle Reef sampled in a mid-depth core near Saskatoon, Saskatchewan (Fig. 1b), with Type 2 dolomite decreasing upwards in abundance. As the two types of dolomite have different  $\delta^{26}\text{Mg}$  values in this core (−1.55‰ for Type 1 and −0.96‰ for Type 2) (Nadeau, 2019; Table S2), vertical gradients in dolomite  $\delta^{26}\text{Mg}$  values may exist within individual Pinnacle Reefs. But as the Lower Member Winnipegosis is entirely composed of Type 2 dolomite below the reefs (Fu et al., 2006), physical mixing cannot explain the basin wide gradient (Nadeau et al., 2019).

Three types of dolomite are recognized in the Red River: (1) burrow; (2) matrix; and (3) saddle dolomite (Qing et al., 2001). Because we restricted sampling to cores with dolomitized burrows and matrix limestone, the possibility that the gradient could reflect geographically controlled mixtures of matrix and burrow dolomite is ruled out. Occasionally, saddle dolomite cements may be found in the burrows (Qing et al., 2001, 2004). However, we think that it is unlikely that burial cements with high  $^{87}\text{Sr}/^{86}\text{Sr}$  ratios (and low  $\delta^{26}\text{Mg}$ ) values mixed with early diagenetic burrow dolomite to create the gradient for two reasons. Firstly, petrographic evidence shows that the burrows contain only minor dolomite cement and that saddle dolomite is rare (Carroll, 1979; Qing et al., 2001, 2004). Secondly, Worsham et al. (2013) reported  $\delta^{26}\text{Mg}$  data from a Red River core where all three dolomite types have nearly the same  $\delta^{26}\text{Mg}$  values at the hand sample scale, which is evidence that later stages of dolomitization overprinted dolomite formed in earlier stages of dolomitization. If the results from this core are representative, there is no isotopic leverage to create isotopic gradients by adjusting the abundances of the three dolomite types in the ‘C’ Member carbonate of the Red River. This finding aligns with dolomite's reputation as a multi-generational mineral (Malone et al., 1996).

### 5.2.4. Cryptic mixing

Fluid-sediment interactions may produce a more subtle form of mixing that can explain gradients in dolomite  $^{87}\text{Sr}/^{86}\text{Sr}$  ratios and  $\delta^{26}\text{Mg}$  values. Li et al. (2015) reported Mg isotope exchange in only a few days between protodolomite and an isotopically enriched Mg tracer solution in

batch reactor experiments at temperatures  $\geq 130^\circ\text{C}$ . The extent to which the  $\delta^{26}\text{Mg}$  value of protodolomite adjusted to the initial  $\delta^{26}\text{Mg}$  value of the fluid depended on the temperature and the mass of Mg in protodolomite compared to that of the fluid. It follows that during burial in a fluid-buffered diagenetic system, the  $\delta^{26}\text{Mg}$  value of early diagenetic protodolomite will gradually change its isotopic composition to that of the migrating fluid, offset by the temperature dependent fractionation factor. But if the burial fluid stops migrating before equilibration is completed, then the dolomite body will record a gradient in  $\delta^{26}\text{Mg}$  values of about the same length-scale as the flow system. Accordingly, basin wide gradients in  $^{87}\text{Sr}/^{86}\text{Sr}$  ratios and  $\delta^{26}\text{Mg}$  values may be preserved in dolomite bodies where the diagenetic conditions governing exchanges of  $^{87}\text{Sr}$  and Mg between migrating fluids and early diagenetic protodolomite change from fluid-buffered to sediment-buffered in the direction of fluid flow. The main assumption is that the burial fluid composition is different from the composition of seawater that initially formed the early diagenetic protodolomite.

### 5.3. Temperature of the ascending fluid

Osadetz et al. (2002) combined stratigraphic constraints with apatite fission track (AFT) thermochronology to construct a thermal history for the Williston Basin. Their analysis revealed anomalous heating in the Late Devonian / Early Carboniferous (Fig. 4a, b). Modeled basement temperatures reached  $120^\circ\text{C}$  during this time in the Baildon well in southern Saskatchewan (~310 million-years-ago) at the paleodepth of 1.85 km (Fig. 4b). This is  $\sim 60^\circ\text{C}$  higher than the burial temperature calculated using the present day geothermal gradient ( $\sim 30^\circ\text{C}/\text{km}$ ) (Lengyel, 2013). The Williston Basin reached its maximum temperature  $\sim 50$  million-years-ago in the Paleogene, up to  $166^\circ\text{C}$  in the basin center (Kuhn et al., 2012), which reflects a normal geothermal gradient for the time. Uplift and erosion have since decreased the depth of the basin to 4.28 km below sea level and the present-day maximum basement temperature of  $\sim 125^\circ\text{C}$  (Gosnold et al., 2012).

Marine carbonate sediments that have been buried for geologically long periods of time experience varying degrees of thermally induced solid-state reordering of  $^{13}\text{C}$ – $^{18}\text{O}$  isotopologues, resulting in higher than expected temperatures from clumped isotope thermometry. These effects become important in calcite at lower temperatures ( $\sim 80$ – $100^\circ\text{C}$ ) (Passey and Henkes, 2012; Henkes et al., 2014; Stolper and Eiler, 2015) than dolomite ( $\sim 150$ – $200^\circ\text{C}$ ) (Lloyd et al., 2018; Stolper et al., 2018). However, as early diagenetic protodolomite is susceptible to recrystallization during burial, dolomite paleotemperatures may also record ambient burial temperatures at the time that recrystallization occurred. Thus, it is difficult to know whether paleotemperatures in dolomite reflect solid-state reordering above  $150$ – $200^\circ\text{C}$  or recrystallization of protodolomite below these temperatures, if the thermal history of the basin is unconstrained. Although temperatures in the center of the Williston Basin exceeded  $150^\circ\text{C}$  for a brief period in the Paleogene, the good agreement between the highest bur-

row dolomite temperature of  $92 \pm 9^\circ\text{C}$  (ND 7362; Tables 2; S3) and the average fluid inclusion temperature for saddle dolomite in the burrows of  $99 \pm 9^\circ\text{C}$  ( $1\sigma$ ) (Qing and Chen, 2010; Fig. 5) is strong evidence that burial did not cause solid-state reordering of dolomite in the Williston Basin, as this would have generated higher clumped isotope temperatures for burrow dolomite than the fluid inclusion temperatures.

Stolper and Eiler (2015) presented a model for thermally induced solid-state reordering of calcite during burial that predicts two stages of reordering between  $75^\circ\text{C}$  and  $150^\circ\text{C}$  for calcite that initially formed in seawater at  $25^\circ\text{C}$ . Partial reordering occurs during the first stage on time scales of a few million years, which is followed by the second stage of slower reordering that may extend for hundreds of millions of years. The model predicts that the paleotemperatures of carbonates formed in seawater will increase by  $\sim 40^\circ\text{C}$  in the first stage, if the ambient burial temperature reaches  $120^\circ\text{C}$ , or increase by  $\sim 50^\circ\text{C}$  in the first stage if the burial temperature climbs to  $150^\circ\text{C}$ . At these temperatures, the second stage of reordering is inconsequential even after 100 million years, and the ‘apparent’ temperature from the first stage of reordering is effectively preserved. The first and second stages of reordering progress more quickly at burial temperatures above  $175^\circ\text{C}$ , and as such, the apparent temperature of deeply buried calcite can increase to the ambient temperature in  $\sim 100$  million years or less. However, the basement temperature in the Williston Basin only reached  $166^\circ\text{C}$  for a brief time in the Paleogene and has since decreased. Therefore, complete thermal reordering of calcite during the second stage is not expected to have occurred. If this interpretation is correct, then the apparent temperature increase will be limited to  $\sim 40$ – $50^\circ\text{C}$  in the deepest buried calcites in the Williston Basin.

First stage reordering of calcite is the most likely reason for the similar paleotemperatures for matrix calcite ( $78$ – $88^\circ\text{C}$ ) and burrow dolomite ( $82$ – $92^\circ\text{C}$ ) in the two deepest Red River cores at 3.83 km and 3.95 km, respectively (Table 2). These calcites are not recrystallized, as indicated

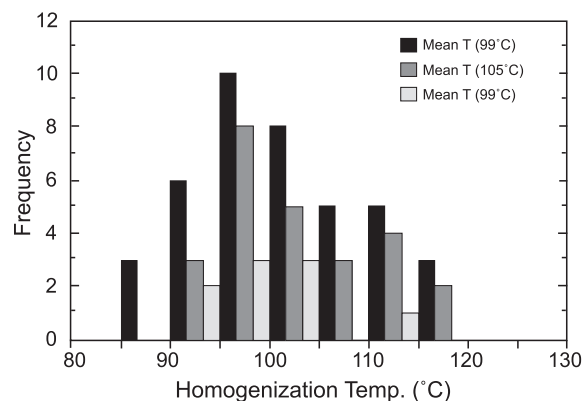


Fig. 5. Frequency histogram depicting homogenization temperatures ( $^\circ\text{C}$ ) of two phase fluid inclusions in the three saddle dolomite cements from the ‘C’ Member carbonate of the Red River (modified from data presented in Qing and Chen, 2010). The sampled wells are from southern Saskatchewan, 5–12 km from the Canada-US border. The weighted mean temperature is  $99.4 \pm 8.5^\circ\text{C}$  (wt. std. dev). Gray-scale bars identify three saddle dolomites.

by their  $^{87}\text{Sr}/^{86}\text{Sr}$  ratios, which are indistinguishable from Late Ordovician seawater ( $0.70795 \pm 0.00005$ ). By contrast, burrow dolomite in the same cores have  $^{87}\text{Sr}/^{86}\text{Sr}$  ratios higher than seawater, consistent with Sr-exchange between ascending fluids and protodolomite. Assuming that matrix calcite formed in seawater at  $35^\circ\text{C}$  and was not significantly recrystallized during early diagenesis, the reordering model of [Stolper and Eiler \(2015\)](#) predicts a first stage apparent calcite temperature of  $85^\circ\text{C}$  ( $=35^\circ\text{C} + 50^\circ\text{C}$ ), which falls in the range of the measured paleotemperatures of  $78\text{--}88^\circ\text{C}$  in the Red River.

The Tyndall Stone from the outcrop belt in Manitoba is the least buried sample of Red River carbonate measured for clumped isotopes in this study (Figs. S2 and S3). The burrow dolomite paleotemperature is  $45 \pm 14^\circ\text{C}$  ( $1\sigma$ ) and the matrix limestone paleotemperature is  $50 \pm 16^\circ\text{C}$  ( $1\sigma$ ) (Table 2). The matrix limestone preserves the  $^{87}\text{Sr}/^{86}\text{Sr}$  ratio of Late Ordovician seawater ( $0.70795 \pm 0.00005$ ), indicating that seawater was either very warm in this setting in the Late Ordovician ([Pratt and Haidl, 2008](#)), or calcite and aragonite recrystallized at this temperature during burial. The outcrop belt is missing  $\sim 100$  m of upper Paleozoic sediment and  $\sim 650$  m of early Mesozoic sediment ([Wright et al., 1994](#)), eroded during uplift of the Williston Basin in the Oligocene ([Kuhn et al., 2012](#)). The restored burial depth is 750 m, which is deep enough to yield the measured temperature of  $50 \pm 16^\circ\text{C}$  ( $1\sigma$ ) during burial. Again, the temperatures for matrix calcite and burrow dolomite give similar temperatures, but for different reasons in the shallow cores compared to the deep cores.

The Red River core ND 8553 is notable in recording different paleotemperatures between the burrow dolomite ( $70 \pm 9^\circ\text{C}$ ,  $1\sigma$ ) and calcite ( $44 \pm 1^\circ\text{C}$ ,  $1\sigma$ ) (Table 2) at 2.4 km depth. The burrow dolomite temperature is very close to the low end of the  $82\text{--}92^\circ\text{C}$  range of burrow dolomite paleotemperatures in the deeper cores (3.83–3.95 km). This is evidence that the ascending fluids were hydrothermal fluids that carried heat upwards in the basin. Indeed, the decrease in dolomite paleotemperature with decreasing depth in the Red River is only  $10.8^\circ\text{C}/\text{km}$  (Table S4), which is unlike any normal geothermal gradient, but consistent with ascending hydrothermal fluids carrying and dissipating heat upwards in the basin.

Hydrothermal fluids are hotter than the rocks that they intrude ([Machel and Lonnee, 2002](#)). In the Williston Basin, this would imply fluid temperatures that were higher than ambient burial temperatures determined from stratigraphic constraints. The strongest evidence that the ascending fluid was hydrothermal is the inverted geothermal gradient implied by the clumped isotope paleotemperature for dolomite in the deepest Winnipegosis core ( $129 \pm 15^\circ\text{C}$ ,  $1\sigma$ ), which is stratigraphically higher than deepest Red River core which gave lower temperatures ( $92 \pm 9^\circ\text{C}$ ). Moreover, the hydrothermal fluid that ascended through the Lower Member Winnipegosis decreased from  $129^\circ\text{C}$  to  $103^\circ\text{C}$  (Table 2, Fig. 4e) between 3.67 km and 1.19 km depth, implying a paleotemperature gradient of  $10.6^\circ\text{C}/\text{km}$  (Table S4). This is nearly identical to the paleotemperature gradient of  $10.8^\circ\text{C}/\text{km}$  in burrow dolomite in the stratigraphically lower Red River.

The similarity in the temperature gradients between the two formations suggests that the clumped isotope temperature of  $129 \pm 15^\circ\text{C}$  for deepest Winnipegosis core is reliable even though the measured samples are mixtures of matrix dolomite and calcite. Earlier we reported the results of a two-component mixing analysis that yielded a much higher apparent temperature for dolomite in this core of  $219 \pm 91^\circ\text{C}$ . However, the uncertainty in the slope of the linear regression (Table S3) is poor, and with the evidence above supporting the lower paleotemperature as it was originally measured, we do not consider the higher paleotemperature determined from the mixing analysis to be reliable. If this interpretation is correct, then the fluid that ascended through the Winnipegosis was  $\sim 40^\circ\text{C}$  hotter at the source than the fluid that ascended through the Red River. This is based on the difference in dolomite paleotemperatures at roughly the same depths in the two studied dolomite bodies. The difference in temperature of the fluids ascending through Red River and Winnipegosis carbonates indicates that the fluids flowed at different speeds, and followed different pathways upwards from the deep structural center of the basin to reach their respective formations, using different down-to-the-basement vertical faults as fluid conduits (discussed below in Section 5.5).

#### 5.4. Cryptic mixing and the $\delta^{26}\text{Mg}$ value of the ascending fluid source

Here we consider a two-stage model for the origin of the Red River and Winnipegosis dolomites that explains the gradients in  $^{87}\text{Sr}/^{86}\text{Sr}$  ratios and  $\delta^{26}\text{Mg}$  values. In the first stage, early diagenetic protodolomite forms by brine reflux, consistent with the presence of evaporite deposits that overlay each dolomite body (Fig. 6b, c). In the second stage, early diagenetic protodolomite is altered to stoichiometric dolomite by ascending  $^{87}\text{Sr}$  and Mg-enriched hydrothermal fluids with diagenetic conditions changing from fluid-buffered to sediment-buffered in the direction of fluid flow (Fig. 6a).

The estimated  $\delta^{26}\text{Mg}$  value for the Mg-bearing fluid that ascended through the Red River burrows is  $-0.65 \pm 0.20\text{‰}$  ( $1\sigma$ ). For this calculation we used the  $\delta^{26}\text{Mg}$  value of  $-1.79\text{‰}$  for the burrow dolomite end-member in the deepest sampled Red River core (ND 7362), which was closest to the fluid source and therefore altered under the most fluid-buffered diagenetic conditions. For the ascending fluid temperature we used  $96 \pm 18^\circ\text{C}$  ( $1\sigma$ ), which is the average of the deepest clumped isotope ( $92 \pm 9^\circ\text{C}$ ,  $1\sigma$ ) and fluid inclusion ( $99 \pm 9^\circ\text{C}$ ,  $1\sigma$ ) temperatures in the Red River cores. The estimated  $\delta^{26}\text{Mg}$  value for the Mg-bearing fluid that ascended through the Lower Member Winnipegosis is of  $-0.93 \pm 0.09\text{‰}$  ( $1\sigma$ ). For this calculation we used the matrix dolomite  $\delta^{26}\text{Mg}$  value of  $-1.89 \pm 0.02\text{‰}$  ( $1\sigma$ ) and the clumped isotope temperature of  $129 \pm 15^\circ\text{C}$  ( $1\sigma$ ) from the deepest Winnipegosis core.

[Banner et al. \(1988\)](#) proposed a two-stage model for the origin of the Burlington-Keokuk dolomite using reaction path modeling of  $\delta^{18}\text{O}$  values,  $^{87}\text{Sr}/^{86}\text{Sr}$  ratios and Sr concentrations. These authors recognized that diagenetic systems can be decoupled, i.e., fluid-buffered for one tracer



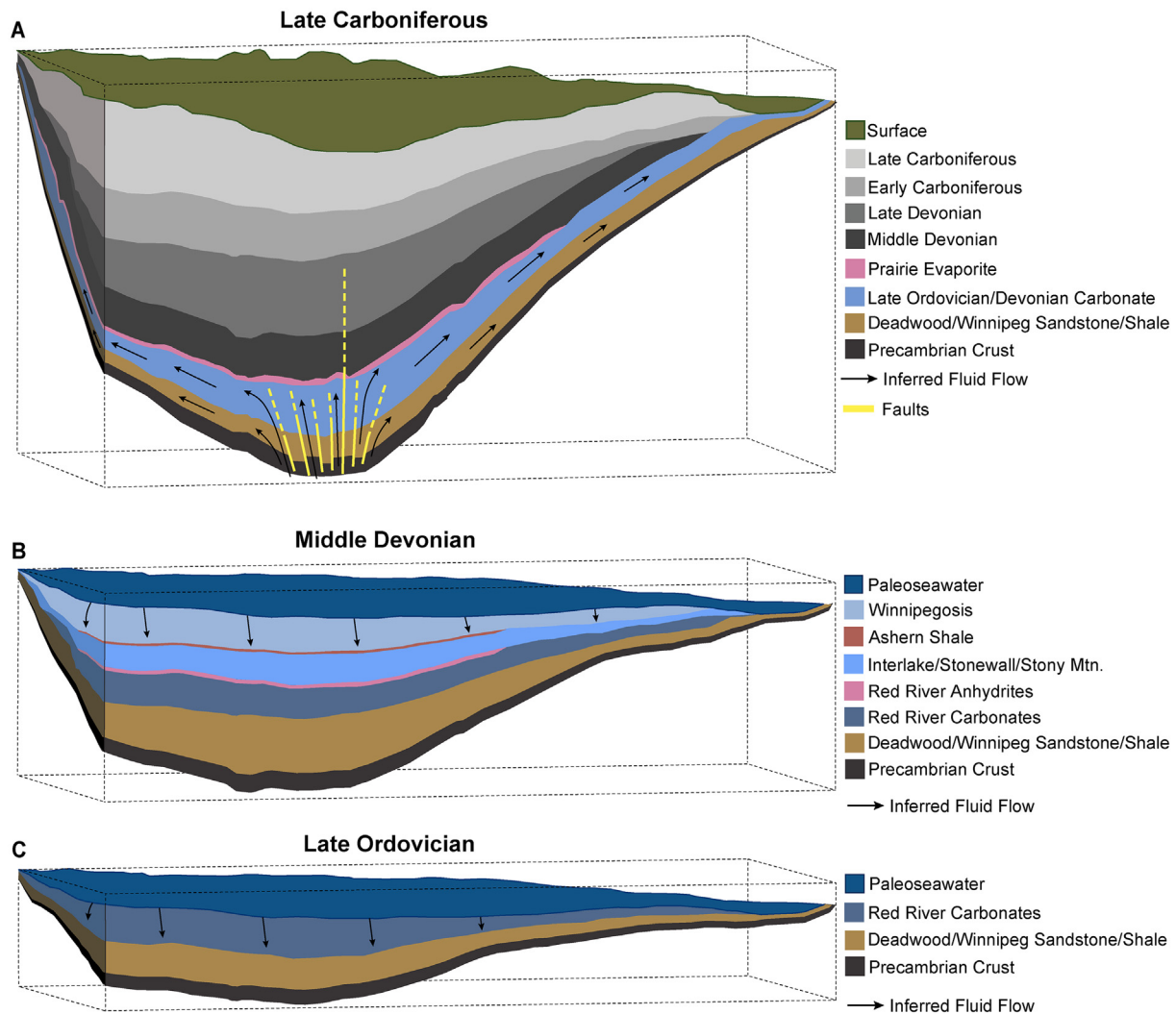


Fig. 6. Two stage model of dolomitization. Stage 1: Early diagenetic formation of protodolomite by evaporatively concentrated seawater (brine reflux model Fig. S1) filtering downward into the studied carbonates B) the Lower Member Winnipegosis and C) the Red River, and A) Stage 2: Alteration of early diagenetic dolomite formed in Stage 1 by younger, ascending  $^{87}\text{Sr}$  and Mg-bearing crustal fluids that used vertical faults to pass into the basal aquifer system of the Williston Basin during the Late Devonian / Early Carboniferous heating event. The longest fault depicts the approximate position of the structural ‘Master Fault’ located west of the Nesson Anticline (Fig. 1b,c). Arrows indicate directions of migrating fluids.

and sediment-buffered for another. Using seawater as the fluid, the relative ease of alteration of some commonly used tracers is  $\delta^{18}\text{O} > ^{87}\text{Sr}/^{86}\text{Sr} > \delta^{26}\text{Mg}_{\text{repl}} > \delta^{26}\text{Mg}_{\text{exch}} > \delta^{44/40}\text{Ca} > \delta^{13}\text{C}$  calculated from mass balance considerations (Banner and Hanson, 1990; Husson et al., 2015). The subscript *repl* represents dolomite formed by the replacement of calcite or aragonite and *exch* represents dolomite formed by replacement of protodolomite.

Mass balance considerations reveal that: (1) more Mg (and more fluid flow) is required to bring early diagenetic protodolomite into isotopic equilibrium with a Mg-bearing fluid than is required to replace calcite or aragonite with dolomite by the same fluid; and (2) a gradient in Mg isotopes in dolomite cannot form in static pore fluids. Because gradients in  $^{87}\text{Sr}/^{86}\text{Sr}$  ratios typically form at lower cumulative fluid–sediment ratios than gradients in  $\delta^{26}\text{Mg}$  values, the discovery of dolomite bodies with gradients in

$^{87}\text{Sr}/^{86}\text{Sr}$  ratios cannot be used to imply that the fluids were dolomitizing fluids. In other words, early diagenetic protodolomite can be altered in Sr isotopes but not in Mg isotopes if the mass of Mg delivered by the fluid was very small compared to the mass of Mg in the protodolomite. These considerations reveal that a multi-proxy approach is important for deciphering the scale and magnitude of subsurface fluid flow in sedimentary basins using tracers that equilibrate between dolomite and fluid at different rates. Magnesium isotopes are crucial in this regard (Ahm et al., 2018) but were not available to earlier workers (Banner et al., 1988).

### 5.5. Drivers of ascending fluid flow

Driving forces of fluid flow in sedimentary basins include topographic relief, fluid overpressure, fluid density,

and rock deformation (Chi and Xue, 2011). Fluid overpressure results from increased fluid volume (heating) and/or decreased pore volume (compaction). Both sources of fluid overpressure may induce ascending fluid flow in sedimentary basins.

Shale compaction may generate ascending fluid flow through pore volume reduction. The Winnipeg shale is a candidate for compaction dewatering in the Williston Basin and it directly underlies the Red River, while the Ashern shale directly underlies the Winnipegosis (Fig. 2). Numerical modeling supports sediment compaction as a mechanism for creating ascending fluid flow in sedimentary basins, but the predicted flow velocities are weak and easily diverted by fluid pressure gradients arising from other sources of fluid flow (Bethke, 1985). Shales can be sources of radiogenic Sr but typically cannot supply the large quantities of Mg required for dolomitization (Wedepohl, 1971). None of the other commonly invoked hydrogeological models of dolomitization are a good fit either (Fig. S1): (1) the Williston Basin is too far from the Rocky Mountains to have been affected by tectonic compaction as a mechanism of fluid pressurization; and (2) there was no topographic relief to drive meteoric waters deeply into the basin before Cretaceous–Paleogene time (Clayton et al., 1966; Chipley and Kyser, 1992; Holmden et al., 1994, 1997; Rostron and Holmden, 2000, 2003; Rostron and Arkadakskiy, 2014). Meteoric flushing of Mg-bearing brines may produce localized dolomitization through upward fluid focussing, but it is a poor recipe for dolomitization at the basin scale (Morrow, 1982; Land, 1985; Machel, 2004).

As the gradients in dolomite  $^{87}\text{Sr}/^{86}\text{Sr}$  ratios and  $\delta^{26}\text{Mg}$  values show, the  $^{87}\text{Sr}$  and Mg-enriched hydrothermal fluids ascended from the deep structural center of the Williston Basin. The more promising mechanisms are therefore those that can create fluid overpressures in the underlying crust through rock deformation (fault-valve action) (Sibson et al., 1975; Sibson, 1994), geothermal heating (magma emplacement or crustal thinning) (Taylor, 1977), and metamorphism (mineral dewatering) (Cathles and Smith, 1983), with fluids transmitted upwards by seismic pumping (Wilson et al., 1990; Oliver et al., 2006; Li et al., 2016; Koeshidayatullah et al., 2020). Hydrocarbon production could have also pressurized deep formation waters in the basin with seals formed by mixtures of gas and water in graded sediment (Hunt, 1990; Powley, 1990; Cathles, 2001). Capillary sealed pressure compartments may pressurize and rupture multiple times to create pulses of ascending fluid flow (Cathles, 2007).

The Williston Basin has a complex block faulted basement topography (Thomas, 1974; Shurr et al., 1994; Anderson, 2011). Fluids likely used these faults to pass into the basal aquifer system of the basin during periods of increased tectonic activity and geothermal heating (Gerhard et al., 1982, 1987; Anderson, 2011; Anna, 2013) (Fig. 1c), such as during the Late Devonian / Early Carboniferous thermal anomaly (Osadetz et al., 2002). Coarsely crystalline masses of saddle dolomite are sometimes found in association with sedimentary basin carbonates crosscut by faults that extend downwards into the underlying crystalline basement rocks (Sharp et al., 2010;

Yapparova et al., 2017). This type of structurally controlled hydrothermal dolomite is easy to recognize and interpret. However, attention has shifted in recent years toward identifying cryptic examples of hydrothermal dolomite in sedimentary basins (Davies and Smith, 2006). In this scenario, vertical faults deliver crustal fluids that pressurize sedimentary aquifers in the deep center of the basin where these faults are numerous, which then causes fluids to migrate up-dip towards the edges of the basin through each aquifer unit. The genetic link between hydrothermal dolomite and faults becomes less obvious as the fluids travel farther from their source and lose heat to the surrounding rocks. Away from the fault, saddle dolomite either does not form or forms in amounts that are less convincingly diagnostic of a structural control governing fluid delivery to the deep aquifers of the basin (Spötl and Pitman, 1998).

Crustal fluids are prime sources of Pb and Zn in Mississippi Valley-Type (MVT) ore deposits (Davies and Smith, 2006). Dolomite is commonly associated with these deposits, indicating that the ore fluids also contained Mg. Only one small showing of MVT mineralization has been reported in the Williston Basin, which is located along the edge of the basin in Manitoba (Bamburak and Klyne, 2004). These ore deposits may have been emplaced into the Williston Basin during the ascending fluid flow event, but since removed by erosion along the edges of the basin.

In summary, vertical faults enabled buoyant fluids to bypass low permeability aquitards that would typically restrict cross-formational fluid flow, pressurizing deep confined carbonate aquifers, such as the Red River and Lower Winnipegosis, and commencing up-dip directed fluid flow towards the edges of the basin (Fig. 6a). In this scenario, the evaporites of the Prairie Evaporite and Red River functioned as aquicludes that contributed to the development of fluid overpressures. If this interpretation is correct, then basin wide gradients in  $^{87}\text{Sr}/^{86}\text{Sr}$  ratios and  $\delta^{26}\text{Mg}$  values should not be found in dolomite bodies located above the Prairie Evaporite. It also follows that dolomite bodies located below the Prairie Evaporite that were not part of this study, such as the ‘A’ and ‘B’ Member dolomite in the Red River, and dolomites belonging to the Silurian Interlake Formation (Fig. 2), will also record basin wide gradients in  $^{87}\text{Sr}/^{86}\text{Sr}$  ratios and  $\delta^{26}\text{Mg}$  values.

## 5.6. Crustal sources of Mg

The mantle contains the most extensive inventory of Mg on Earth with a uniform  $\delta^{26}\text{Mg}$  value of  $-0.25 \pm 0.04\text{‰}$  ( $2\sigma$ ) (Teng et al., 2010). Positive gravity anomalies in the crust below the Williston Basin are interpreted as bodies of ultramafic rock belonging to the Thompson Nickel Belt which outcrops in Manitoba, but extends southwards beneath the Phanerozoic cover in North Dakota where it passes under the Williston Basin (Fig. 1c, Green et al., 1979; Klasner and King, 1986). The Thompson Nickel Belt contains remnants of ancient oceanic crust and serpentinized upper mantle rocks obducted during collisions of island arcs with the Superior Craton during the ca. 1.85 Ga Trans-Hudson Orogeny. Serpentinite has been reported in one of the twenty drill cores that recovered basement rocks

below the Williston Basin in North Dakota (Klasner and King, 1986; Luther, 1988).

Magnesium isotopes are not fractionated by serpentinization, but subsequent reactions involving serpentine and CO<sub>2</sub> rich fluids produce an association of talc, magnesite, and quartz (referred to as listwanite) that does fractionate Mg isotopes. Talc preferentially sequesters heavy Mg isotopes while magnesite takes up light Mg isotopes (Beinlich et al., 2014). In Section 5.4, we determined that the fluid that ascended through the Red River burrows carried reactive Mg with a  $\delta^{26}\text{Mg}$  value of  $-0.65 \pm 0.20\text{‰}$  ( $1\sigma$ ), which falls in the range of  $\delta^{26}\text{Mg}$  values reported in magnesite ( $-0.66\text{‰}$  to  $-1.07\text{‰}$ ) of the Linnajavri Ultramafic Complex, Norway (Beinlich et al., 2014). Carbonation of ultramafic rocks proceeds in stages (Hansen et al., 2005). Robertson et al. (2019) observed that when serpentine is nearly completely consumed by carbonation, fluid pH drops and a portion of the magnesite dissolves, thus creating a fluid that is capable of dolomitization, and enriched in light Mg isotopes. Listwanitization of serpentine is a process that could have generated large supplies of reactive Mg in the ultramafic crust below the Williston Basin, implying large fluxes of carbon dioxide during the anomalous heating event.

Chlorite is a Mg-bearing mineral that is commonly associated with hydrothermal alteration of mafic igneous rocks, and mafic minerals in felsic igneous rocks such as biotite ( $-0.29$  to  $-0.12\text{‰}$ ) and amphibole ( $-0.32$  to  $-0.14\text{‰}$ ) (Liu et al., 2010; Ryu et al., 2011; Teng, 2017). The similar  $\delta^{26}\text{Mg}$  values to mafic igneous rocks ( $-0.25\text{‰}$ ) implies limited Mg isotope fractionation during magmatic processes (Liu et al., 2010). However, a much broader range of  $\delta^{26}\text{Mg}$  values is found in chlorite ( $-0.78$  to  $-1.82\text{‰}$ ) (Ryu et al., 2011; Kimmig et al., 2018), pointing to metasomatic fluids as another source of fractionated Mg isotopes in the crust. In addition, chlorite preferentially releases light isotopes of Mg during the early stages of its dissolution (Ryu et al., 2011). Two cores intersecting basement rocks beneath the Williston Basin in North Dakota contain chloritic schists (Luther, 1988).

The source of Mg has bearing on the  $^{87}\text{Sr}/^{86}\text{Sr}$  ratio of the ascending hydrothermal fluid. If it is chlorite, then chloritization of biotite could explain the high  $^{87}\text{Sr}/^{86}\text{Sr}$  ratio of the fluid. But if magnesite is the source, a mantle-like  $^{87}\text{Sr}/^{86}\text{Sr}$  ratio of  $\sim 0.7035$  is expected, which is inconsistent with the orientation of the  $^{87}\text{Sr}/^{86}\text{Sr}$  gradient in dolomite in the Williston Basin. In this case, radiogenic Sr would have to be acquired on the flow path between ultramafic sites of serpentine carbonation in the Thompson Nickel Belt, and the vertical faults in the structural center of the basin that channelled these fluids upwards into the basin. This is feasible considering that the Thompson Nickel Belt is located to the east of where many of the vertical faults are located. The basement rocks that directly underlay the Williston Basin belong to the Trans-Hudson and Wyoming structural provinces, which contain felsic igneous rocks ranging in age from 1.85 to 3.6 Ga, with exceedingly high  $^{87}\text{Sr}/^{86}\text{Sr}$  ratios in Rb-bearing minerals like biotite and orthoclase. Additional considerations are the distribution coefficient for Sr in magnesite which is  $< 0.5$  at  $100^\circ\text{C}$

(Lindner et al., 2019), and  $^{87}\text{Sr}$  additions from the basal sandstones and shales of the Winnipeg and Deadwood formations that the fluids had to bypass (*via* fractures and faults) to reach the Red River and Winnipegosis aquifers.

### 5.7. Timing of ascending fluid flow

Koehler et al. (1997) reported two groupings of K-Ar ages in sylvite in the Prairie Evaporite: one at  $\sim 50$  Ma, and the other at  $\sim 300$  Ma (Wardlaw, 1968; Baadsgard, 1987; Koehler et al., 1997) (Fig. 4d). Both ages are lower than the depositional age of the evaporite, indicating that younger fluids dissolved and recrystallized evaporite minerals (Chipley and Kyser, 1992) on at least two occasions in the geological past. Paleomagnetic directions in hematite inclusions in the evaporite minerals give broadly similar ages to the geochronological ages (Koehler et al., 1997; Cioppa, 2003; Szabo and Cioppa, 2006). In addition, Koehler et al. (1997) combined  $\delta^{18}\text{O}$  values in hematite with fluid inclusion temperatures in halite to estimate  $\delta^{18}\text{O}$  values for waters in equilibrium with hematite ranging between  $0.0\text{‰}$  and  $-8\text{‰}$  (VSMOW). Waters with similar  $\delta^{18}\text{O}$  values are common in formations above the potash mines in the Prairie Evaporite (Wittrup and Kyser, 1990), and trapped waters in halite, with  $\delta^{18}\text{O}$  values ranging between  $-6\text{‰}$  and  $-15\text{‰}$ , and  $\delta\text{D}$  values ranging between  $-70\text{‰}$  and  $-141\text{‰}$  (Chipley and Kyser, 1992). These low values indicate mixing between deep formation waters and Cretaceous or younger meteoric waters with very low  $\delta\text{D}$  ( $-150\text{‰}$ ) and  $\delta^{18}\text{O}$  ( $-19\text{‰}$ ) values.

Meteoric waters with these signatures did not appear in the Williston Basin before the onset of the Sevier Orogeny along the western margin of North America in the Late Jurassic. By the early Cretaceous, the mountains were high enough to cause a dramatic lowering of  $\delta\text{D}$  and  $\delta^{18}\text{O}$  values in precipitation throughout the study region (Clayton et al., 1966; Wittrup and Kyser, 1990; Holmden et al., 1994; 1997). The high elevation head in the mountains permitted meteoric waters to deeply infiltrate the Western Canada Sedimentary Basin (Nesbitt and Muehlenbachs, 1994). Younger mountain uplifts of Paleogene age, such as the Black Hills in North Dakota, delivered meteoric waters with similarly low  $\delta\text{D}$  and  $\delta^{18}\text{O}$  values into the Williston Basin along its southwestern margin (Knechtel, 1959; Marvin et al., 1980; Bachu and Hitchon, 1996; Rostron and Holmden, 2000, 2003; Jensen et al., 2006; Rostron and Arkadaskiy, 2006). The deepest formation waters in the Williston Basin have very high  $\delta^{18}\text{O}$  values of  $+5$  to  $+10\text{‰}$  in the present day, indicating that they have likely not mixed with isotopically lighter Cretaceous and younger meteoric waters (Benn and Rostron, 1998; Rostron and Holmden, 2000, 2003; Jensen et al., 2006; Rostron and Arkadaskiy, 2006). The calculated  $\delta^{18}\text{O}$  values for the hydrothermal fluids that ascended through the Red River ( $+2.6 \pm 1.7\text{‰}$ ) and Winnipegosis ( $+7.1 \pm 1.5\text{‰}$ ) formations (Table 2) also show little evidence for having mixed with Cretaceous or younger meteoric waters, indicating that these fluids must have ascended before the Sevier uplift of the Western Cordillera, thus pointing to anomalous heating in the Late Devonian / Early Carboniferous as the most

likely age of the ascending fluid flow event in the Williston Basin.

Many MVT deposits were formed in sedimentary basins across North America between the Late Devonian and Carboniferous (Christensen et al., 1996) (Fig. 4c), implying that ascending fluid flow occurred in many sedimentary basins at around the same time. Kominz and Bond (1991) proposed that North America drifted into a geoid low in the Late Devonian, and that the resulting stress reactivated basement faults beneath sedimentary basins that in turn caused subsidence, geothermal heating, and widespread flooding of the craton that continued into the Carboniferous. Late Paleozoic remagnetizations have been reported in the Williston Basin (Koehler et al., 1997) and in other sedimentary basins in North America (McCabe and Elmore, 1989). The late Paleozoic was also a time of widespread contractional orogeny along the margins of North America, specifically the Appalachian and Ouachita orogenies on the eastern and southeastern margins (Thomas, 1985), and the Antler Orogeny on the western margin (Speed and Sleep, 1982). Far-field tectonic effects may have played a role in remobilizing basement structures beneath the Williston Basin that in turn provided conduits for pressurized fluids to ascend through the crust and into the basin.

### 5.8. Implications for reconstructing the $^{26}\text{Mg}$ -history of seawater

Despite being a diagenetic mineral, dolomite has the potential to record the  $\delta^{26}\text{Mg}$  value of seawater at near-surface temperatures in seawater-buffered early diagenetic systems (Holland and Zimmermann, 2000; Tipper et al., 2006; Higgins and Schrag, 2010, 2012; Fantle and Higgins, 2014; Ahm et al., 2018; Murray et al., 2020). A key consideration is the slow reaction rates that govern carbonate precipitation during diagenesis (Jacobson and Holmden, 2008; Fantle et al., 2010; Fantle and Higgins, 2014; Higgins and Schrag, 2015; Gothmann et al., 2017). This allows protodolomite to form in isotopic equilibrium with seawater. Primary marine calcite and aragonite are less attractive archives due to strong and variable kinetic isotope effects arising from their comparatively rapid precipitation rates (Wombacher et al., 2011; Li et al., 2012). Limestones complicate things further by being mixtures of fractionated biologically-produced carbonates of uncertain biological affinity, with metastable aragonite and high-magnesium calcite that are susceptible to recrystallization during diagenesis. Additionally, limestone successions must be carefully screened for small amounts of 'background dolomite' that can effectively skew the primary carbonate  $\delta^{26}\text{Mg}$  signature (Kimmig and Holmden, 2017; Murray et al., 2020).

This study shows that dolomite is also not a perfect archive for recording seawater  $\delta^{26}\text{Mg}$  values. Although dolomites located beneath evaporite deposits would seem like ideal targets for reconstructing the  $^{26}\text{Mg}$ -history of seawater, early diagenetic reflux dolomites are mostly altered in the Williston Basin. Ironically, evaporites contributed to dolomite alteration by turning the underlying carbonate

units into confined aquifers that could channel Mg-bearing hydrothermal fluids towards the edges of the basin during the ascending fluid flow event. In the Williston Basin, the least altered dolomites are located near the edges of the basin. Knowing the geometry and history of fluid flow can help to locate the least altered dolomites in other sedimentary basins.

The least altered burrow dolomite in the Red River belongs to the Tyndall Stone sample collected from a quarry in the Manitoba outcrop belt (Fig. S2) with a  $\delta^{26}\text{Mg}$  value of  $-1.46\text{‰}$  (Table 1). The matrix limestone records the  $^{87}\text{Sr}/^{86}\text{Sr}$  ratio of Late Ordovician seawater, but the burrow dolomite records a higher ratio, indicating that Mg and  $^{87}\text{Sr}$ -enriched fluids flowed past the present day erosional edge of the basin during the ascending fluid flow event. Approximately 750 m of sediment is missing from the outcrop belt where the Tyndall Stone was sampled (Wright et al., 1994; Kuhn et al., 2012). Using the basin wide gradient of increasing burrow-dolomite  $\delta^{26}\text{Mg}$  values with decreasing depth, the  $\delta^{26}\text{Mg}$  value for the least altered burrow dolomite is  $-1.41 \pm 0.03\text{‰}$  (1 $\sigma$ ) (Table S5), which corresponds to a paleosurface that is 750 m higher and farther away from the center of the Williston Basin than the Tyndall Stone quarry. The result is not significantly different from the  $\delta^{26}\text{Mg}$  value of the burrow dolomite in the Tyndall Stone, due to the slope uncertainty of the trend in  $\delta^{26}\text{Mg}$  vs. depth (Table S5). Applying the same technique to the Lower Member Winnipegosis dolomite yields a projected least altered dolomite with a  $\delta^{26}\text{Mg}$  value of  $-1.43 \pm 0.06\text{‰}$  (1 $\sigma$ ). This value is close to the average  $\delta^{26}\text{Mg}$  value for Type 1 dolomite in the Pinnacle Reefs from the Upper Member Winnipegosis, which preserves the Middle Devonian seawater  $^{87}\text{Sr}/^{86}\text{Sr}$  ratio and has an average  $\delta^{26}\text{Mg}$  value of  $-1.55 \pm 0.01\text{‰}$  (1 $\sigma$ ) (Table S2; Nadeau et al., 2019).

Assuming a nominal paleotemperature of 35°C for shallow water epeiric seas located near the equator in the early Paleozoic (Finnegan et al., 2011; Henkes et al., 2018; Goldberg et al., 2021), the least altered  $\delta^{26}\text{Mg}$  value for burrow dolomite in the Red River yields an inferred seawater  $\delta^{26}\text{Mg}$  value of  $+0.23 \pm 0.10\text{‰}$  for Late Ordovician seawater. The least altered  $\delta^{26}\text{Mg}$  value for matrix dolomite in the Lower Member Winnipegosis yields an inferred seawater  $\delta^{26}\text{Mg}$  value of  $+0.21 \pm 0.10\text{‰}$  for Middle Devonian seawater. Type 1 dolomite in the Upper Member Winnipegosis Pinnacle Reef yields  $+0.09 \pm 0.11\text{‰}$  for Middle Devonian seawater. The results are plotted on a seawater Mg isotope evolution diagram (Fig. 7) with a model that predicts the secular evolution of seawater  $\delta^{26}\text{Mg}$  values (Li et al., 2015). The model is computed from estimates of changing dolomite abundances with time in marine carbonates of Phanerozoic age (Wilkinson and Algeo, 1989). The model assumes that dolomite forms during early diagenesis using seawater as the Mg source.

The model is in good agreement with estimates for early Paleozoic seawater using Williston Basin dolomites that are the least altered. Dolomites from other sedimentary basins are reported for comparison, including: (1) the Early Ordovician St. George Group dolomite from the Laurentian Basin in Newfoundland (Azmy et al., 2013); (2) Late



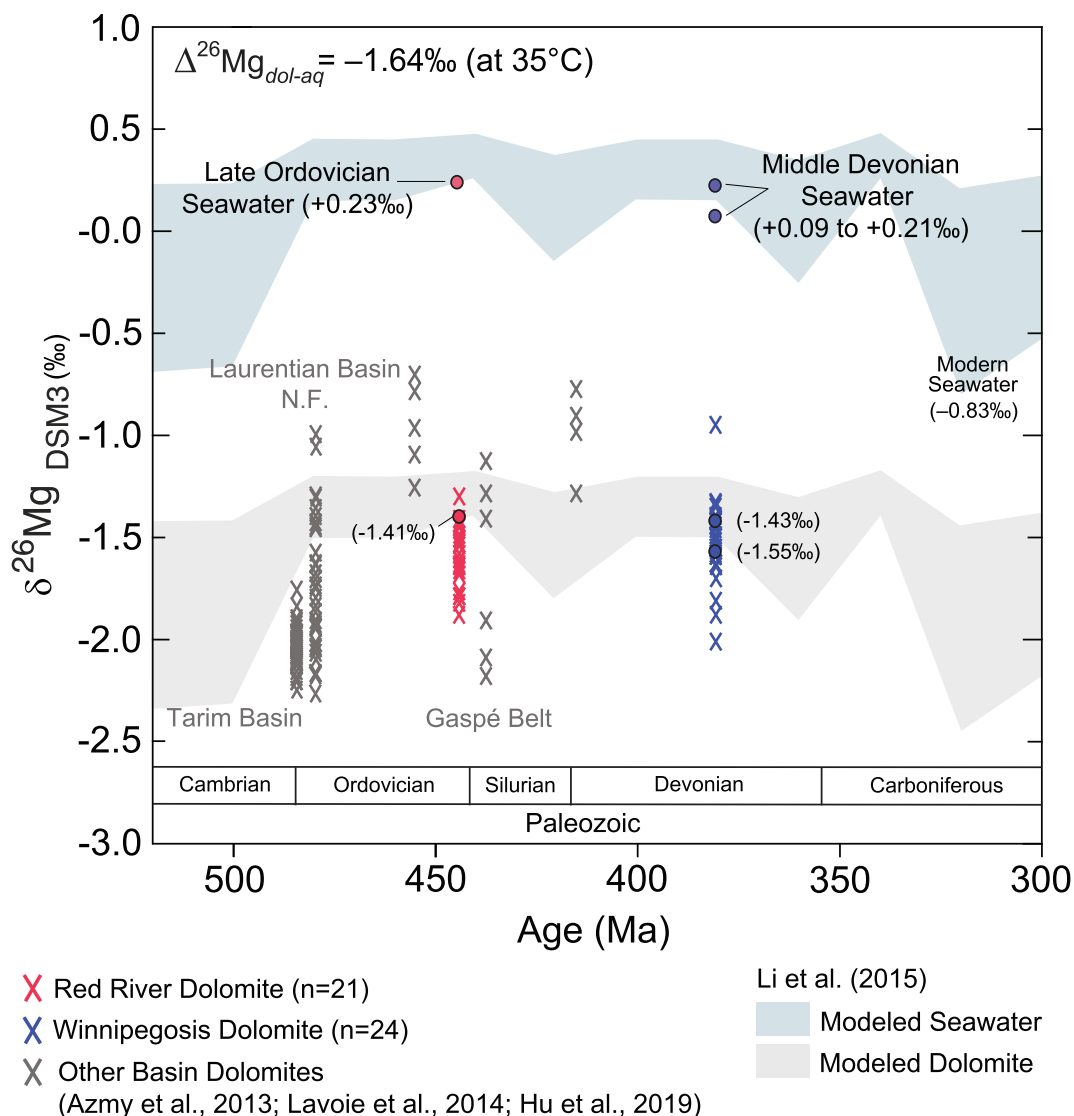


Fig. 7. The  $\delta^{26}\text{Mg}$  values in dolomite from this study and the literature compared to the early Paleozoic portion of a model of the proposed secular evolution of seawater  $\delta^{26}\text{Mg}$  by Li et al., 2015) and the corresponding evolution of early diagenetic dolomite formed using seawater as a Mg source, at 35°C. Nearly all dolomite measured in this study of the Williston Basin is altered. The best estimate for Late Ordovician seawater and two best estimates for Middle Devonian seawater are, however, consistent with the evolution curve predicted by the model, while the altered data are inconsistent with the model and plot below the secular curve. Literature data from other sedimentary basins with known or suspected hydrothermal activity also plot below the secular curve (Azmy et al., 2013; Lavoie et al., 2014; Hu et al., 2019). The dolomites are plotted according to the ages of the formations that host the dolomite, rather than the actual ages of the dolomite, which is usually unknown.

Ordovician, Silurian and Devonian dolomites from the Gaspé Belt in Newfoundland (Lavoie et al., 2014); and (3) early Cambrian dolomite from the Tarim Basin in China (Hu et al., 2019). Most of these dolomites plot below the secular curve, implying that dolomites in other sedimentary basins have likely also experienced complex histories of fluid flow involving Mg-bearing fluids that altered early diagenetic protodolomite during burial.

## 6. CONCLUSIONS

Basin wide gradients in  $^{87}\text{Sr}/^{86}\text{Sr}$  ratios and  $\delta^{26}\text{Mg}$  values in dolomite identify the deep structural center of the Williston Basin as a source of  $^{87}\text{Sr}$  and Mg-enriched fluid

that ascended and altered early diagenetic protodolomite. Although ascending fluids with high  $^{87}\text{Sr}/^{86}\text{Sr}$  ratios were identified in earlier studies of a few cores, the magnitude of the fluid flow event could not be fully appreciated before basin wide mapping was undertaken in this study. Moreover, it could not be determined in earlier studies whether the ascending fluids were dolomitizing fluids that carried reactive Mg, as this necessitates analysis of  $\delta^{26}\text{Mg}$  values in addition to  $^{87}\text{Sr}/^{86}\text{Sr}$  ratios. Clumped isotope thermometry provided evidence that the ascending fluids were hydrothermal. The highest inferred  $\delta^{18}\text{O}$  value of the ascending hydrothermal fluid is +7.1‰, implying highly saline waters with no evidence of mixing with isotopically light Cretaceous or younger meteoric waters. This con-

strains the timing of ascending fluid flow to have occurred before mountain uplift happened during the Sevier Orogeny, which created topographic relief, high elevation head, and low meteoric water  $\delta D$  and  $\delta^{18}O$  values in the Late Jurassic / Early Cretaceous that could infiltrate and mix with formation waters in the Williston Basin. It is hypothesized that down-to-the-basement vertical faults located in the structural center of the Williston Basin served as conduits for passing crustal fluids upwards into the deep center of the basin during anomalous heating in the Late Devonian / Early Carboniferous, pressurizing deep confined aquifers and initiating up-dip directed fluid flow. Although both studied dolomite bodies lie below basin scale evaporites, indicating that dolomitization likely occurred initially using Mg supplied by evaporatively concentrated seawater, nearly all of the early diagenetic dolomite was subsequently altered during burial by ascending flows of reactive Mg from the crust.

The ascending fluids were heterogenous in flow rate and temperature and transferred heat to the surrounding rocks as they migrated upwards. Our best estimate for the  $\delta^{26}Mg$  value of the ascending fluid is  $-0.65 \pm 0.20\text{‰}$  ( $1\sigma$ ). This is a good match for two crustal sources of Mg: (1) magnesite formed by carbonation of serpentinite ( $-0.7\text{‰}$  to  $-1.1\text{‰}$ ); and (2) chlorite formed by crustal metasomatism ( $-0.78$  to  $-1.8\text{‰}$ ). Ultramafic rocks belonging to the Thompson Nickel Belt pass beneath the Williston Basin in North Dakota, indicating that carbonation of serpentinite is a plausible source of reactive Mg for dolomitization in the Williston Basin.

Dolomites are a potentially important archive for reconstructing the  $^{26}Mg$ -history of seawater. The basis for this claim is that most dolomites preserved in sedimentary basins formed under fluid-buffered conditions during early diagenesis using seawater as a Mg source. However, in this study we have shown that early diagenetic dolomites are susceptible to alteration during burial in sedimentary basins by Mg-bearing fluids ascending from the crust. The least altered dolomites are located near the shallowly buried edges of the basin. We use the basin scale gradients in dolomite  $\delta^{26}Mg$  values with depth to obtain best estimates for the  $\delta^{26}Mg$  values for Late Ordovician and Middle Devonian seawater of  $+0.23\text{‰}$  and  $+0.21\text{‰}$ , respectively, assuming a paleotemperature of early diagenetic dolomite formation of  $35^{\circ}C$ . These nearly identical estimates are much higher than the  $\delta^{26}Mg$  value for modern seawater of  $-0.83\text{‰}$ , implying higher rates of dolomite formation in the early Paleozoic.

### Declaration of Competing Interest

The authors declare that they have no known competing financial interests or personal relationships that could have appeared to influence the work reported in this paper.

### ACKNOWLEDGEMENTS

This work is supported by the Geological Society of America Graduate Student Research Grant, Saskatchewan Ministry of Energy and Resources, and NSERC Discovery Grant. We thank

the Saskatchewan Ministry of Energy and Resources Subsurface Geological Laboratory, the Manitoba Mineral Resources Midland Sample and Core Library, and the Wilson M. Laird Core and Sample Library in Grand Forks, ND for granting core viewing and sampling privileges. Many thanks to Jim Rosen and Mosa Nasreen for laboratory assistance, as well as Sandra Timsic for software assistance, Julien Kimmig for help in the core laboratories, and Julien Kimmig and Cathrin Hagey for editing. Many thanks to Hairuo Qing for assistance sampling in the core lab and for discussions pertaining to dolomitization in the Williston Basin. Thank you to Ted Huston and Jing Chen for performing the elemental analyses. We also thank three journal reviewers whose comments helped to improve the presentation.

### APPENDIX A. SUPPLEMENTARY MATERIAL

Supplementary data to this article can be found online at <https://doi.org/10.1016/j.gca.2021.06.006>.

### REFERENCES

- Adams J. E. and Rhodes M. L. (1960) Dolomitization by seepage refluxion. *Bull. Am. Assoc. Petrol. Geol.* **44**, 1912–1920.
- Ahm A.-S. C., Bjerrum C. J., Blättler C. L., Swart P. K. and Higgins J. A. (2018) Quantifying early marine diagenesis in shallow-water carbonate sediments. *Geochim. Cosmochim. Acta* **236**, 140–159.
- Anderson F. J. (2011) Structural relationships between surface lineaments and basement faulting in the northeastern Williston Basin. In *The Bakken-Three Forks Petroleum System in the Williston Basin* (eds. J. W. Robinson, J. A. LeFever and S. B. Gaswirth). Rocky Mountain Assoc. Geol., pp. 376–392.
- Anna L. O. (2013) Geologic assessment of undiscovered oil and gas in the Williston Basin Province, Montana, North Dakota, and South Dakota. In *Assessment of Undiscovered Oil and Gas Resources of the Williston Basin Province of North Dakota, Montana, and South Dakota. U.S. Geological Survey Digital Data Series 69–W* (ed. U.S. Geological Survey Williston Basin Province Assessment Team), p. 71.
- Arvidson R. S. and Mackenzie F. T. (1999) The dolomite problem; control of precipitation kinetics by temperature and saturation state. *Am. J. Sci.* **299**, 257–288.
- Azmy K., Lavoie D., Wang Z., Brand U., Al-Aasm I., Jackson S. and Girard I. (2013) Magnesium-isotope and REE compositions of Lower Ordovician carbonates from eastern Laurentia: Implications for the origin of dolomites and limestones. *Chem. Geol.* **356**, 64–75.
- Baadsgaard H. (1987) Rb-Sr and K-Ca isotope systematics in minerals from potassium horizons in the Prairie Evaporite Formation, Saskatchewan, Canada. *Chem. Geol.* **66**, 1–15.
- Bachu S. and Hitchon B. (1996) Regional-scale flow of formation waters in the Williston Basin. *Am. Assoc. Petrol. Geol. Bull.* **80**, 248–264.
- Baker P. A., Gieskes J. M. and Elderfield H. (1982) Diagenesis of carbonates in deep-sea sediments—Evidence from Sr/Ca ratios and interstitial dissolved  $Sr^{2+}$  data. *J. Sed. Petrol.* **52**, 71–82.
- Bamburak J. D. and Klyne K. (2004) A possible new Mississippi Valley-type mineral occurrence near Pemmican Island in the north basin of Lake Winnipegosis, Manitoba (NTS 63B12 and 13, 63C9 and 16). In *Report of Activities 2004*. Manitoba Industry, Economic Development and Mines, Manitoba Geological Survey, pp. 266–278.
- Banner J. L. and Hanson G. N. (1990) Calculation of simultaneous isotopic and trace element variations during water-rock inter-

- action with applications to carbonate diagenesis. *Geochim. Cosmochim. Acta* **54**, 3123–3137.
- Banner J. L., Hanson G. N. and Meyers W. J. (1988) Rare earth element and Nd isotopic variations in regionally extensive dolomites from the Burlington-Keokuk Formation (Mississippian); implications for REE mobility during carbonate diagenesis. *J. Sed. Res.* **58**, 415–432.
- Beinlich A., Mavromatis V., Austrheim H. and Oelkers E. H. (2014) Inter-mineral Mg isotope fractionation during hydrothermal ultramafic rock alteration – Implications for the global Mg-cycle. *Earth Planet. Sci. Lett.* **392**, 166–176.
- Benn A. A. and Rostron B. J. (1998) Regional hydrochemistry of Cambrian to Devonian aquifers. In *the Williston Basin, Canada - U.S.A., Eighth International Williston Basin Symposium* (eds. J. E. Christopher, C. F. Gilboy, D. F. Paterson and S. L. Bend). Sask. Geol. Soc. Spec. Pub. No. 13, pp. 238–246.
- Bethke C. M. (1985) A numerical model of compaction-driven groundwater flow and heat transfer and its application to the paleohydrology of intracratonic basins. *J. Geophys. Res.* **90**, 6817–6828.
- Brand W. A., Assonov S. S. and Coplen T. B. (2010) Correction for the  $^{17}\text{O}$  interference in  $\delta(^{13}\text{C})$  measurements when analyzing  $\text{CO}_2$  with stable isotope mass spectrometry. *Pure Appl. Chem.* **82**, 1719–1733.
- Burrus J., Osadetz K. G., Wolf S., Doligez B., Visser K. and Dearborn D. (1996) A two-dimensional regional basin model of Williston Basin hydrocarbon systems. *Am. Assoc. Pet. Geol. Bull.* **80**, 265–291.
- Carroll W. K. (1979) Depositional environments and paragenetic porosity controls, upper Red River Formation, North Dakota. *North Dakota Geological Survey, Report of Investigations* **66**, 51.
- Cathles L. M. (2001) Capillary seals as a cause of pressure compartmentation in sedimentary basins. In *Petroleum Systems of Deep-Water Basins: Global and Gulf of Mexico Experience Proceedings of the Gulf Coast Section Society of Economic Paleontologists and Mineralogists Foundation, 21st Annual Bob F. Perkins Research Conference*, pp. 561–572.
- Cathles L. M. (2007) Changes in sub-water table fluid flow at the end of the Proterozoic and its implications for gas pulsars and MVT lead-zinc deposits. *Geofluids* **7**, 209–226.
- Cathles L. M. and Smith A. T. (1983) Thermal constraints on the formation of Mississippi Valley-type lead-zinc deposits and their implications for episodic basin dewatering and deposit genesis. *Econ. Geol.* **78**, 983–1002.
- Chi G. and Xue C. (2011) An overview of hydrodynamic studies of mineralization. *Geosci. Front.* **2**, 423–438.
- Chi G. and Xue C. (2011) An overview of hydrodynamic studies of mineralization. *Geosci. Front.* **2**, 423–438.
- Chipley D. and Kyser T. K. (1992) Preservation of ancient basinal fluids in halite fluid inclusions. In *Proceedings of the 7th International Symposium on Water/Rock Interaction* (eds. J. Kharaka and A. S. Maest). International Association of Geochemistry and Cosmochemistry and Alberta Research Council, Sub-Group on Water-Rock Interaction, Edmonton, AB, Canada, pp. 1105–1108.
- Christensen J. N., Halliday A. N., Leigh K. E., Randell R. N. and Kesler S. E. (1996) Direct dating of sulfides by Rb-Sr: A critical test using the Polaris Mississippi Valley-type Zn-Pb deposit. *Geochim. Cosmochim. Acta* **59**, 5191–5196.
- Cioppa M. T. (2003) Magnetic evidence for the nature and timing of fluid migration in the Watrous Formation, Williston Basin, Canada: a preliminary study. *J. Geochem. Explor.* **78–79**, 349–354.
- Clayton R. N., Friedman I., Graf D. L., Mayeda T. K., Meents W. F. and Shimp N. F. (1966) The origin of saline formation waters. *J. Geophys. Res.* **71**, 3869–3882.
- Craig H. (1957) Isotopic standards for carbon and oxygen and correction factors for mass- spectrometric analysis of carbon dioxide. *Geochim. Cosmochim. Acta* **12**, 133–149.
- Daëron M., Blamart D., Peral M. and Affek H. (2016) Absolute isotopic abundance ratios and the accuracy of  $\Delta_{47}$  measurements. *Chem. Geol.* **442**, 83–96.
- Davies G. R. and Smith, Jr., L. B. (2006) Structurally controlled hydrothermal dolomite reservoir facies: an overview. *Am. Assoc. Petrol. Geol. Bull.* **90**, 1641–1690.
- Defliese W. F. and Lohmann K. C. (2015) Non-linear mixing effects on mass-47  $\text{CO}_2$  clumped isotope thermometry: patterns and implications. *Rapid Commun. Mass Spectrom.* **29**, 901–909.
- Dennis K. J., Affek H. P., Passey B. H., Schrag D. P. and Eiler J. M. (2011) Defining an absolute reference frame for 'clumped' isotope studies of  $\text{CO}_2$ . *Geochim. Cosmochim. Acta* **75**, 7117–7131.
- Fantle M. S., Maher K. M. and DePaolo D. J. (2010) Isotopic approaches for quantifying the rates of marine burial diagenesis. *Rev. Geophys.* **48**, 38.
- Fantle M. S. and Higgins J. (2014) The effects of diagenesis and dolomitization on Ca and Mg isotopes in marine platform carbonates: Implications for the geochemical cycles of Ca and Mg. *Geochim. Cosmochim. Acta* **142**, 458–481.
- Finnegan S., Bergmann K., Eiler J. M., Jones D. S., Fike D. A., Eisenman I., Hughes N. C., Tripathi A. K. and Fischer W. W. (2011) The magnitude and duration of Late Ordovician-Early Silurian glaciation. *Science* **331**, 903–906.
- Fu Q., Qing H. and Bergman K. M. (2006) Dolomitization of the Middle Devonian Winnipegosis carbonates in south-central Saskatchewan, Canada. *Sedimentology* **53**, 825–848.
- Galy A., Belshaw N., Halicz L. and O'Nions R. (2001) High precision measurement of magnesium-isotopes by multiple-collector inductively coupled plasma mass spectrometry. *Int. J. Mass Spectrom.* **208**, 89–98.
- Galy A., Bar-Matthews M., Halicz L. and O'Nions R. K. (2002) Mg isotopic composition of carbonate: insight from speleothem formation. *Earth Planet. Sci. Lett.* **201**, 105–115.
- Galy A., Yoffe O., Janney P., Williams R., Cloquet C., Alard O., Halicz L., Wadhwa M., Hutcheon I., Ramon E. and Carignan J. (2003) Magnesium-isotope heterogeneity of the isotopic standard SRM980 and new reference materials for magnesium isotope-ratio measurements. *J. Anal. Atom. Spect.* **18**, 1352–1356.
- Gendzwill D. J. (1978) Winnipegosis mounds and Prairie Evaporite Formation of Saskatchewan-seismic study. *Am. Assoc. Petrol. Geol. Bull.* **62**, 73–86.
- Gendzwill D. J. and Wilson N. L. (1987) Form and distribution of Winnipegosis mounds in Saskatchewan. In *Williston Basin: Anatomy of a cratonic oil province* (eds. J. A. Peterson, D. Kent, S. B. Anderson, R. H. Pilatzke and M. W. Longman). Rocky Mountain Association of Geologists, pp. 109–117.
- Gerhard L. C., Anderson S. B., LeFever J. A. and Carlson C. G. (1982) Geological development, origin, and energy mineral resources of the Williston Basin, North Dakota. *Am. Assoc. Petrol. Geol. Bull.* **66**, 989–1020.
- Gerhard L. C., Anderson S. B. and LeFever J. A. (1987) Structural history of the Nesson Anticline, North Dakota. In *Williston Basin: anatomy of a cratonic oil province* (ed. M. W. Longman). Rocky Mountain Association of Geologists, pp. 337–353.
- Geske A., Goldstein R. H., Mavromatis V., Richter D. K., Buhl D., Kluge T., John C. M. and Immenhauser A. (2015) The magnesium isotope ( $^{26}\text{Mg}$ ) signature of dolomites. *Geochim. Cosmochim. Acta* **149**, 131–151.
- Gingras A., Pemberton S. G., Muchlenbachs K. and Machel H. (2004) Conceptual models for burrow-related, selective dolomitization with textural and isotopic evidence from the Tyndall Stone, Canada. *Geobiology* **2**, 21–30.

- Goldberg S. L., Present T. M., Finnegan S. and Bergmann K. D. (2021) A high-resolution record of early Paleozoic climate. *Proc. Natl. Acad. Sci.* **118**(e2013083118), 8p.
- Gosnold W. D., McDonald M. R., Klenner R. and Merriam D. (2012) Throstratigraphy of the Williston Basin. *GRC Trans.* **36**, 663–670.
- Gothmann A. M., Stolarski J., Adkins J. F. and Higgins J. A. (2017) A Cenozoic record of seawater Mg isotopes in well-preserved fossil corals. *Geology* **45**, 1039–1042.
- Green A. C., Cumming G. L. and Cedarwell D. (1979) Extension of the Superior-Churchill boundary zone into southern Canada. *Can. J. Earth Sci.* **16**, 1691–1701.
- Gregg J. M., Bish D. L., Kaczmarek S. E. and Machel H. G. (2015) Mineralogy, nucleation and growth of dolomite in the laboratory and sedimentary environment: A review. *Sedimentology* **62**, 1749–1769.
- Hansen L. D., Dipple G. M., Gordon T. M. and Kellett D. A. (2005) Carbonated serpentinite (listwanite) at Atlin, British Columbia: a geological analogue to carbon dioxide sequestration. *Canad. Mineral.* **43**, 225–239.
- Hardie L. A. (1987) Dolomitization: a critical view of some current views. *J. Sed. Res.* **57**, 166–183.
- He B., Olack G. A. and Colman A. S. (2012) Pressure baseline correction and high-precision CO<sub>2</sub> clumped-isotope ( $\Delta_{47}$ ) measurements in bellows and micro-volume modes. *Rap. Comm. Mass Spec.* **26**, 2837–2853.
- Henkes G. A., Passey B. H., Grossman E. L., Shenton B. J., Pérez-Huerta A. and Yancey T. E. (2014) Temperature limits for preservation of primary calcite clumped isotope paleotemperatures. *Geochim. Cosmochim. Acta* **139**, 362–382.
- Henkes G. A., Passey B. H., Grossman E. L., Shenton B. J., Yancey T. E. and Pérez-Huerta A. (2018) Temperature evolution and the oxygen isotope composition of Phanerozoic oceans from carbonate clumped isotope thermometry. *Earth Planet. Sci. Lett.* **490**, 40–50.
- Higgins J. A. and Schrag D. P. (2010) Constraining magnesium cycling in marine sediments using magnesium isotopes. *Geochim. Cosmochim. Acta* **74**, 5039–5053.
- Higgins J. A. and Schrag D. P. (2012) Records of Neogene seawater chemistry and diagenesis in deep-sea carbonate sediments and pore fluids. *Earth Planet. Sci. Lett.* **357–358**, 386–396.
- Higgins J. A. and Schrag D. P. (2015) The Mg isotopic composition of Cenozoic seawater – evidence for a link between Mg-clays, seawater Mg/Ca, and climate. *Earth Planet. Sci. Lett.* **416**, 73–81.
- Higgins J. A., Blättler C. L., Lundstrom E. A., Santiago-Ramos D. P., Akhtar A. A., Ahm A.-S. C., Bialik O., Holmden C., Bradbury H., Murray S. T. and Swart P. K. (2018) Mineralogy, early marine diagenesis, and the chemistry of shallow-water carbonate sediments. *Geochim. Cosmochim. Acta* **220**, 512–534.
- Holland H. D. and Zimmermann H. (2000) The dolomite problem revisited. *Int. Geol. Rev.* **42**, 481–490.
- Holmden C., Muehlenbachs K. and Creaser R. A. (1994) Paleosalinity and paleoenvironment of the Early Cretaceous ostracode sea. In *Calgary: Western Canadian and International Expertise*. CSPG Spec. Pub. pp. 313–314.
- Holmden C., Creaser R. A. and Muehlenbachs K. (1997) Paleosalinities in ancient brackish water systems determined by <sup>87</sup>Sr/<sup>86</sup>Sr ratios in carbonate fossils: A case study from the Western Canada Sedimentary Basin. *Geochim. Cosmochim. Acta* **61**, 2105–2118.
- Holmden C. (2009) Ca isotope study of Ordovician dolomite, limestone, and anhydrite in the Williston Basin: implications for subsurface dolomitization and local Ca cycling. *Chem. Geol.* **268**, 180–188.
- Horita J. (2014) Oxygen and carbon isotope fractionation in the system dolomite–water–CO<sub>2</sub> to elevated temperatures. *Geochim. Cosmochim. Acta* **129**, 111–124.
- Hu Z., Hu W., Liu C., Sun F., Liu Y. and Li W. (2019) Conservative behavior of Mg isotopes in massive dolostones: From diagenesis to hydrothermal reworking. *Sed. Geol.* **381**, 65–75.
- Hunt J. M. (1990) Generation and migration of petroleum from abnormally pressured fluid compartments. *Am. Assoc. Petrol. Geol. Bull.* **74**, 1–12.
- Huntington K. W., Eiler J. M., Affek H. P., Guo W., Bonifacie M., Yeung L. Y., Thiagarajan N., Passey B., Tripathi A., Daëron M. and Came R. (2009) Methods and limitations of ‘clumped’ CO<sub>2</sub> isotope ( $\Delta_{47}$ ) analysis by gas-source isotope ratio mass spectrometry. *J. Mass Spec.* **44**, 1318–1329.
- Husinec A. (2016) Sequence stratigraphy of the Red River Formation, Williston Basin, USA: Stratigraphic signature of the Ordovician Katian greenhouse to icehouse transition. *Mar. Petrol. Geol.* **77**, 487–506.
- Husson J. M., Higgins J. A., Maloof A. C. and Schoene B. (2015) Ca and Mg isotope constraints on the origin of Earth’s deepest  $\delta^{13}\text{C}$  excursion. *Geochim. Cosmochim. Acta* **160**, 243–266.
- Iampien H. T. and Rostron B. J. (2000) Hydrogeochemistry of pre-Mississippian brines, Williston Basin, Canada–USA. *J. Geochem. Explor.* **69–70**, 29–35.
- Illing L. V. (1959) Deposition and diagenesis of some upper palaeozoic carbonate sediments in Western Canada. *Fifth World Petrol. Cong. Proc.*, 23–52.
- Jacobson A. D. and Holmden C. (2008)  $\delta^{44}\text{Ca}$  evolution in a carbonate aquifer and its bearing on the equilibrium isotope fractionation factor for calcite. *Earth Planet. Sci. Lett.* **270**, 349–353.
- Jensen G. K. S., Rostron B. J., Duke M. J. M. and Holmden C. (2006) Bromine and stable isotopic profiles of formation waters from potash mine-shafts, Saskatchewan, Canada. *J. Geochem. Explor.* **89**, 170–173.
- Jin J. and Bergman K. M. (1999) Sequence stratigraphy of the Middle Devonian Winnipegosis carbonate-prairie evaporite transition, southern Elk Point Basin. *Carbonates and Evaporites* **14**, 64–83.
- Jin J. and Bergman K. M. (2001) Revised stratigraphy of the Middle Devonian (Givetian) Winnipegosis carbonate–Prairie Evaporite transition, Elk Point Group, southern Saskatchewan. *Bull. Can. Petrol. Geol.* **49**, 441–457.
- Jin J., Harper D. A. T., Rasmussen J. A. and Sheehan P. M. (2012) Late Ordovician massive-bedded Thalassinoides ichnofacies along the palaeoequator of Laurentia. *Palaeogeogr. Palaeoclimatol. Palaeoecol.* **367–368**, 73–88.
- Jones B. and Luth R. W. (2002) Dolostones from Grand Cayman, British West Indies. *J. Sed. Res.* **72**, 559–569.
- Jones L. J. (1965) The Middle Devonian Winnipegosis Formation of Saskatchewan. *Sask. Dep. Miner. Resour. Rep.* **98**, 101p.
- Kaczmarek S. E. and Sibley D. F. (2011) On the evolution of dolomite stoichiometry and cation order during high-temperature synthesis experiments: an alternative model for the geochemical evolution of natural dolomites. *Sed. Geol.* **240**, 30–40.
- Kendall A. C. (1975) The Middle Devonian Winnipegosis and lower Prairie Evaporite formations of the commercial potash areas. In *Summ. Rep. Inv. Sask. Geol. Surv.* (eds. J. E. Christopher and R. Macdonald), pp. 61–65.
- Kendall A. C. (1976) The Ordovician carbonate succession (Bighorn Group) of southeastern Saskatchewan. *Sask. Dep. Miner. Resour. Rep.* **180**, 185p.
- Kendall A. C. (1977) Origin of dolomite mottling in Ordovician limestones from Saskatchewan and Manitoba. *Bull. Can. Petrol. Geol.* **25**, 480–504.



- Kendall A. C. (1984) Origin and Geometry of Red River Dolomite Reservoirs, Western Williston Basin: Discussion. *Amer. Assoc. Petrol. Geol. Bull.* **68**, 776–784.
- Kim S.-T. and O'Neil J. R. (1997) Equilibrium and nonequilibrium oxygen isotope effects in synthetic carbonates. *Geochim. Cosmochim. Acta* **61**, 3461–3475.
- Kimmig S. R. and Holmden C. (2017) Multi-proxy geochemical evidence for primary aragonite precipitation in a tropical-shelf 'calcite sea' during the Hirnantian glaciation. *Geochim. Cosmochim. Acta* **206**, 254–272.
- Kimmig S. R., Holmden C. and Bélanger N. (2018) Biogeochemical cycling of Mg and its isotopes in a sugar maple forest in Québec. *Geochim. Cosmochim. Acta* **230**, 60–82.
- Kinsman D. J. J. (1969) Interpretation of  $\text{Sr}^{2+}$  concentrations in carbonate minerals and rocks. *J. Sed. Petrol.* **39**, 486–508.
- Klasner J. S. and King E. R. (1986) Precambrian basement geology of North and South Dakota. *Can. J. Earth Sci.* **23**, 1083–1102.
- Knauth L. P. and Beeunas M. A. (1986) Isotope geochemistry of fluid inclusions in Permian halite with implications for the isotopic history of ocean water and the origin of saline formation waters. *Geochim. Cosmochim. Acta* **50**, 419–433.
- Knechtel M. M. (1959) Stratigraphy of the Little Rocky Mountains and encircling foothills, Montana. *U.S. Geol. Surv. Bull.* **1072-N**, 723–752.
- Koehler G., Kyser T. K., Enkin R. and Irving E. (1997) Paleomagnetic and isotopic evidence for the diagenesis and alteration of evaporites in the Paleozoic Elk Point Basin, Saskatchewan, Canada. *Can. J. Earth Sci.* **34**, 1619–1629.
- Koeshidayatullah A., Corlett H., Stacey J., Swart P. K., Boyce A. and Hollis C. (2020) Origin and evolution of fault-controlled hydrothermal dolomitization fronts: A new insight. *Earth Planet. Sci. Lett.* **541** 116291.
- Kohm J. A. and Loudon R. O. (1978) Ordovician Red River Formation, eastern Montana and western North Dakota: relationships between lithofacies and production. In *The economic geology of the Williston Basin: Williston Basin Symposium* (eds. D. Estelle and R. Miller). Montana Geol. Soc. 24th Ann. Field Conf. Guide, pp. 99–117.
- Kohout F. A. (1967) Ground-water flow and the geothermal regime of the Floridian plateau. *Trans. Gulf Coast Assoc. Geol. Soc.* **17**, 339–354.
- Kominz M. A. and Bond G. C. (1991) Unusually large subsidence and sea-level events during middle Paleozoic time: new evidence supporting mantle convection models for supercontinent assembly. *Geology* **19**, 56–60.
- Kuhn P. P., di Primio R., Hill R., Lawrence J. R. and Horsfield B. (2012) Three-dimensional modeling study of the low-permeability petroleum system of the Bakken Formation. *Am. Assoc. Petrol. Geol. Bull.* **96**, 1867–1897.
- Land L. S. (1980) The isotopic and trace element geochemistry of dolomite: the state of the art. In *Concepts and Models of Dolomitization*, vol. 28 (ed. D. H. Zenger). SEPM Spec. Pub., pp. 87–110.
- Land L. S. (1985) The origin of massive dolomite. *J. Geol. Ed.* **33**, 112–125.
- Land L. S. (1998) Failure to precipitate dolomite at 25°C from dilute solution despite 1000-fold oversaturation after 32 years. *Aquat. Geochem.* **4**, 361–368.
- Lavoie D., Jackson S. and Girard I. (2014) Magnesium isotopes in high-temperature saddle dolomite cements in the lower Paleozoic of Canada. *Sed. Geol.* **305**, 58–68.
- Leach D., Bradley D., Lewchuk M. T., Symons D. T. A., de Marsily G. and Brannon J. (2001) Mississippi Valley-type lead-zinc deposits through geological time: implications from recent age-dating research. *Mineral. Dep.* **36**, 711–740.
- Lengyel T. (2013) Geothermics of the Phanerozoic strata of Saskatchewan Master dissertation. University of Alberta, p. 248.
- Li W., Chakraborty S., Beard B. L., Romanek C. S. and Johnson C. M. (2012) Magnesium isotope fractionation during precipitation of inorganic calcite under laboratory conditions. *Earth Planet. Sci. Lett.* **333–334**, 304–316.
- Li W., Beard B. L., Li C., Xu H. and Johnson C. M. (2015) Experimental calibration of Mg isotope fractionation between dolomite and aqueous solution and its geological implications. *Geochim. Cosmochim. Acta* **157**, 164–181.
- Li Z., Chi G. and Bethune K. M. (2016) The effects of basement faults on thermal convection and implications for the formation of unconformity-related uranium deposits in the Athabasca Basin, Canada. *Geofluids* **16**, 729–751.
- Lindner M., Saldi G. D., Stumpp D., Schott J. and Jordan G. (2019) On the effect of aqueous strontium on magnesite growth. *Chem. Geol.* **510**, 1–9.
- Ling M. X., Sedaghatpour F., Teng F. Z., Hays P. D., Strauss J. and Sun W. D. (2011) Homogenous magnesium isotopic composition of seawater: an excellent geostandard for Mg isotope analysis. *Rap. Commun. Mass Spectrom.* **25**, 2828–2836.
- Liu S.-A., Teng F.-Z., He Y., Ke S. and Li S. (2010) Investigation of magnesium isotope fractionation during granite differentiation: implication for Mg isotopic composition of the continental crust. *Earth Planet. Sci. Lett.* **297**, 646–654.
- Lloyd M. K., Ryb U. and Eiler J. M. (2018) Experimental calibration of clumped isotope reordering in dolomite. *Geochim. Cosmochim. Acta* **242**, 1–20.
- Lobdell F. K. (1984) Age and depositional history of the Middle Devonian Ashern Formation in the Williston Basin, Saskatchewan and North Dakota. In *Sask. Geol. Soc. Spec. Pub. No. 7: Oil and gas in Saskatchewan, Proceedings of a Symposium*, pp. 5–12.
- Longman M. W. and Haidl F. M. (1996) Cyclic deposition and development of porous dolomites in the Upper Ordovician Red River Formation, Williston Basin. In *Paleozoic Systems of the Rocky Mountain Region* (eds. M. W. Longman and M. D. Sonnenfeld). Rocky Mountain Section, SEPM. Soc. Sed. Geol., pp. 29–46.
- Longman M. W., Fertil T. G. and Glennie J. S. (1983) Origin and geometry of Red River dolomite reservoirs, western Williston Basin. *Amer. Assoc. Petrol. Geol. Bull.* **67**, 744–771.
- Luther K. C. (1988) Proterozoic structures in north-central North Dakota: a gravity study Master dissertation. University of North Dakota, p. 184.
- Machel H. G. (2004) Concepts and models of dolomitization: a critical reappraisal. In *The Geometry and Petrogenesis of Dolomite Hydrocarbon Reservoirs*, vol. 235 (eds. C. J. R. Braithwaite, G. Rizzi and G. Darke). Geol. Soc. London, Spec. Pub., pp. 7–63.
- Machel H. G. and Anderson J. H. (1989) Pervasive subsurface dolomitization of the Nisku Formation in central Alberta. *J. Sed. Petrol.* **59**, 891–911.
- Machel H. G. and Lonnee J. (2002) Hydrothermal dolomite—a product of poor definition and imagination. *Sed. Geol.* **152**, 163–171.
- Maiklem W. R. (1971) Evaporative drawdown—a mechanism for water-level lowering and diagenesis in the Elk Point Basin. *Bull. Can. Petrol. Geol.* **19**, 485–501.
- Malone M. J., Baker P. A. and Burns S. J. (1996) Recrystallization of dolomite: an experimental study from 50–200°C. *Geochim. Cosmochim. Acta* **60**, 2189–2207.
- Martindale W., Erkmen U., Metcalfe D. and Potts E. (1991) Winnipegosis buildups of the Hitchcock area, southeastern

- Saskatchewan—a case study. In *Sixth International Williston Basin Symposium*, pp. 47–63.
- Marvin R. F., Hearn, Jr., B. C., Mehnert H. H., Naeser C. W., Zartman R. E. and Lindsay D. A. (1980) Late Cretaceous–Paleocene–Eocene igneous activity in north central Montana. *Isotopes* **29**, 5–25.
- Matthews A. and Katz A. (1977) Oxygen isotope fractionation during the dolomitization of calcium carbonate. *Geochim. Cosmochim. Acta* **41**, 1431–1438.
- McCabe C. and Elmore R. D. (1989) The occurrence and origin of Late Paleozoic remagnetization in the sedimentary rocks of North America. *Reviews of Geophysics* **4**, 471–494.
- Montañez I. P. (1994) Late diagenetic dolomitization of Lower Ordovician, Upper Knox carbonates: a record of the hydrodynamic evolution of the Southern Appalachian Basin. *Am. Assoc. Petrol. Geol. Bull.* **78**, 1210–1239.
- Morrow D. W. (1982) Diagenesis 2; Dolomite – Part 2 Dolomitization models and ancient dolostones. *Geosci. Can.* **9**, 95–107.
- Murphy E. C., Nordeng S. H., Juenker B. J. and Hoganson J. W. (2009) North Dakota stratigraphic column. ND Geological Survey, Misc. Series, p. 91.
- Murray S. T. and Swart P. K. (2017) Evaluating formation fluid models and calibrations using clumped isotope paleothermometry on Bahamian dolomites. *Geochim. Cosmochim. Acta* **206**, 73–93.
- Murray S. T., Arienzo M. M. and Swart P. K. (2016) Determining the  $\Delta_{47}$  acid fractionation in dolomites. *Geochim. Cosmochim. Acta* **174**, 42–53.
- Murray S. T., Higgins J. A., Holmden C., Lu C. and Swart P. K. (2020) Geochemical fingerprints of dolomitization in Bahamian carbonates: Evidence from sulphur, calcium, magnesium and clumped isotopes. *Sedimentology* **68**, 1–29.
- Nadeau M. D. (2019) Deciphering the dolomitization history of the Lower Member Winnipegosis carbonates: basin-scale gradients in magnesium and strontium isotopes identify the deep structural center of the Williston Basin as a source of reactive magnesium Master dissertation. University of Saskatchewan, p. 99.
- Nadeau M. D., Kimmig S. R. and Holmden C. (2019) Basin-wide gradients in dolomite  $\delta^{26}\text{Mg}$  and  $^{87}\text{Sr}/^{86}\text{Sr}$  identify the structural centre of the Williston Basin as a source of magnesium for dolomitization of the Middle Devonian Winnipegosis Formation. *Summ. Rep. Inv. Sask. Geol. Surv.* **1**, 21p.
- Nesbitt B. E. and Muehlenbachs K. (1994) Paleohydrology of the Canadian Rockies and origins of brines, Pb–Zn deposits and dolomitization in the Western Canada Sedimentary Basin. *Geology* **22**, 243–246.
- Nielsen P., Swennen R. and Keppens E. (1994) Multiple-step recrystallization within massive ancient dolomite units: an example from the Dinant of Belgium. *Sedimentology* **41**, 567–584.
- Oliver J. (1986) Fluids expelled tectonically from orogenic belts: their role in hydrocarbon migration and other geologic phenomena. *Geology* **14**, 99–102.
- Oliver N. H. S., McLellan J. G., Hobbs B. E., Cleverley J. S., Ord J. S. and Feltrin L. (2006) Numerical models of extensional deformation, heat transfer, and fluid flow across basement-cover interfaces during basin-related mineralization. *Econ. Geol.* **101**, 1–31.
- Osadetz K. G., Kohn B. P., Feinstein S. and O’Sullivan P. B. (2002) Thermal history of Canadian Williston basin from apatite fission-track thermochronology—implications for petroleum systems and geodynamic history. *Tectonophysics* **349**, 221–249.
- Passey B. H. and Henkes G. A. (2012) Carbonate clumped isotope bond reordering and geospeedometry. *Earth Planet. Sci. Lett.* **351–352**, 223–236.
- Peng Y., Shen B., Lang X.-G., Huang K.-J., Chen J.-T., Yan Z., Tang W.-B., Ke S., Ma H.-R. and Li F.-B. (2016) Constraining dolomitization by Mg isotopes: a case study from partially dolomitized limestones of the middle Cambrian Xuzhuang Formation, North China. *Geochem. Geophys. Geosyst.* **17**, 1109–1129.
- Perrin N. A. (1982) Environment of Deposition of Winnipegosis Formation (Middle Devonian), Williston Basin, North Dakota. *Am. Assoc. Petrol. Geol. Bull.* **66**, 616–617.
- Powley D. E. (1990) Pressures and hydrogeology in petroleum basins. *Earth Sci. Rev.* **29**, 215–226.
- Pratt B. R. and Haidl F. M. (2008) Microbial patch reefs in Upper Ordovician Red River strata, Williston Basin, Saskatchewan: signal of heating in a deteriorating epeiric sea. In *Dynamics of Epeiric Seas* (Eds. B. R. Pratt and C. Holmden) *Geol. Assoc. Can. Spec. Paper* **48**, 303–340.
- Pu R. and Qing H. (2003) Pool characterization of Ordovician Midale field: Implication for Red River play in northern Williston basin, southeastern Saskatchewan, Canada. *Am. Assoc. Petrol. Geol. Bull.* **87**, 1699–1715.
- Qing H. and Chen D. Z. (2010) Non-hydrothermal saddle dolomite: petrological and geochemical evidence from the Ordovician Yeoman Formation, Southeastern Saskatchewan, Canada. *Acta Sedimentol. Sinica* **28**, 980–986.
- Qing H. and Mountjoy E. W. (1992) Large-scale fluid flow in the Middle Devonian Presqu’île barrier, Western Canada Sedimentary Basin. *Geology* **20**, 903–906.
- Qing H. and Mountjoy E. W. (1994) Formation of coarsely crystalline, hydrothermal dolomite reservoirs in the Presqu’île barrier, Western Canada Sedimentary Basin. *Am. Assoc. Petrol. Geol. Bull.* **78**, 55–77.
- Qing H., Barnes C. R., Buhl D. and Veizer J. (1998) The strontium isotopic composition of Ordovician and Silurian brachiopods and conodonts: Relationships to geological events and implications for coeval seawater. *Geochim. Cosmochim. Acta* **62**, 1721–1733.
- Qing H., Kent D. and Bend S. (2001) Preliminary results of isotopic geochemistry of Ordovician Red River carbonates, subsurface of southeastern Saskatchewan: implication for process of dolomitization and diagenetic modification of dolomites. *Summ. Rep. Inv. Sask. Geol. Surv.* **1**, 3–9.
- Qing H., Bend S., Kent D. and Haidl F. (2004) Petrography and isotopic geochemistry of Ordovician Red River dolomites, Midale Pool and 3-8-1-11W2, southeastern Saskatchewan. In *Proceedings of Dolomites: The Spectrum: Mechanisms, Models, Reservoir Development Can. Soc. Petrol. Geol., Seminar and Core Conference, Calgary, Alberta, Canada*, pp. 1–19.
- Reinson G. E. and Wardlaw N. C. (1972) Nomenclature and Stratigraphic Relationships, Winnipegosis and Prairie Evaporite Formations. Central Saskatchewan. *Bull. Can. Petrol. Geol.* **20**, 301–320.
- Ren M. and Jones B. (2017) Spatial variations in the stoichiometry and geochemistry of Miocene dolomite from Grand Cayman: implications for the origin of island dolostone. *Sed. Geol.* **348**, 69–93.
- Robertson H., Corlett H., Hollis C., Kibblewhite T. and Whitaker F. (2019) Listwanitization as a source of Mg for dolomitization: field evaluation in Atlin, British Columbia. *Goldschmidt Conference Abstract* 2848, Barcelona.
- Rostron B. J. and Holmden C. (2000) Fingerprinting formation-waters using stable isotopes, Midale Area, Williston Basin, Canada. *J. Geochem. Explor.* **69–70**, 219–223.
- Rostron B. J. and Holmden C. (2003) Regional variations in oxygen isotopic compositions in the Yeoman and Duperow aquifers, Williston basin (Canada-USA). *J. Geochem. Explor.* **78–79**, 337–341.

- Rostron B. and Arkadakskiy S. (2014) Fingerprinting “stray” formation fluids associated with hydrocarbon exploration and production. *Elements* **10**, 285–290.
- Ryu J.-S., Jacobson A. D., Holmden C., Lundstrom C. and Zhang Z. (2011)  $\delta^{44/40}\text{Ca}$ ,  $\delta^{44/42}\text{Ca}$ , and  $\delta^{26/24}\text{Mg}$  geochemistry of granite weathering at pH = 1 and T = 25°C: power-law processes and the relative reactivity of minerals. *Geochim. Cosmochim. Acta* **75**, 6004–6026.
- Schauer A. J., Kelson J., Saenger C. and Huntington K. W. (2016) Choice of  $^{17}\text{O}$  correction affects clumped isotope ( $\Delta_{47}$ ) values of  $\text{CO}_2$  measured with mass spectrometry. *Rap. Comm. Mass Spec.* **30**, 2607–2616.
- Schmitt A. D., Gangloff S., Cobert F., Lemarchand D., Stille P. and Chabaux F. (2009) High performance automated ion chromatography separation for Ca isotope measurements in geological and biological samples. *J. Anal. At. Spectrom.* **24**, 1089–1097.
- Sharp I., Gillespie P., Morsalnezhad D., Taberner C., Karpuz R., Vergés J., Horbury A., Pickard N., Garland J. and Hunt D. (2010) Stratigraphic architecture and fracture-controlled dolomitization of the Cretaceous Khani and Bangestan groups: an outcrop case study, Zagros Mountains, Iran. In *Mesozoic and Cenozoic Carbonate Systems of the Mediterranean and the Middle East: Stratigraphic and Diagenetic Reference Models*, vol. 329 (eds. F. S. P. Van Buchem, K. D. Gerdes and M. Esteban). Geol. Soc. London, pp. 343–396.
- Shields M. J. and Brady P. V. (1995) Mass balance and fluid flow constraints on regional-scale dolomitization, Late Devonian, Western Canada Sedimentary Basin. *Bull. Can. Petrol. Geol.* **43**, 371–392.
- Shurr G. W., Hammond R. H. and Bretz R. F. (1994) Cretaceous paleotectonism and postdepositional tectonism in south-central South Dakota: an example of epeirogenic tectonism in continental lithosphere. In *Perspectives on the eastern margin of the Cretaceous Western Interior Basin*, vol. 287 (eds. G. W. Shurr, G. A. Ludvigson and R. H. Hammond). Geol. Soc. Am. Special Paper, pp. 237–256.
- Sibley D. F., Nordeng S. H. and Borkowski M. L. (1994) Dolomitization kinetics in hydrothermal bombs and natural settings. *J. Sed. Res.* **64**, 630–637.
- Sibson R. H. (1994) Crustal stress, faulting and fluid flow. In *Geofluids: origin, migration and evolution of fluids in sedimentary basins* (Ed. J. Parnell) Geol. Soc. Spec. Pub. **78**, 69–84.
- Sibson R. H., Moore J. Mc and Rankin A. H. (1975) Seismic pumping—a hydrothermal fluid transport mechanism. *J. Geol. Soc. London* **131**, 653–659.
- Simms M. (1984) Dolomitization by groundwater-flow systems in carbonate platforms. *Trans. Gulf Coast Assoc. Geol. Soc.* **34**, 411–420.
- Speed R. C. and Sleep N. H. (1982) Antler orogeny and foreland basin: a model. *Geol. Soc. Am. Bull.* **93**, 815–828.
- Spötl C. and Pitman J. K. (1998) Saddle (baroque) dolomite in carbonates and sandstones: a reappraisal of a burial-diagenetic concept. In *Carbonate Cementation in Sandstones* (Ed. S. Morad) Int. Assoc. Sedimentol. Spec. Pub. **26**, 437–460.
- Stolper D. A. and Eiler J. M. (2015) The kinetics of solid-state isotope-exchange reactions for clumped isotopes: A study of inorganic calcites and apatites from natural and experimental samples. *Am. J. Sci.* **315**, 363–411.
- Stolper D. A., Eiler J. M. and Higgins J. A. (2018) Modeling the effects of diagenesis on carbonate clumped-isotope values in deep- and shallow-water settings. *Geochim. Cosmochim. Acta* **227**, 264–291.
- Swart P. K., Burns S. J. and Leder J. J. (1991) Fractionation of the stable isotopes of oxygen and carbon in carbon dioxide during the reaction of calcite with phosphoric acid as a function of temperature and technique. *Chem. Geol.* **86**, 89–96.
- Swart P. K., Murray S. T., Staudigel P. T. and Hodell D. A. (2019) Oxygen isotopic exchange between  $\text{CO}_2$  and phosphoric acid: Implications for the measurement of clumped isotopes in carbonates. *Geochem. Geophys. Geosys.* **20**, 3730–3750.
- Szabo E. and Cioppa M. T. (2006) Multiple magnetization events in the Red River carbonates, Williston Basin, Canada: evidence for fluid-flow? *J. Geochem. Explor.* **89**, 384–388.
- Taylor H. P. (1977) Water/rock interactions and the origin of  $\text{H}_2\text{O}$  in granitic batholiths. *J. Geol. Soc.* **133**, 509–558.
- Taylor R. D., Leach D. L., Bradley D. C. and Pisarevsky S. A. (2009) Compilation of mineral resource data for Mississippi Valley-type and clastic-dominated sediment-hosted lead-zinc deposits. In *U.S. Geol. Survey Open-File Report 2009–1297*. U. S. Geol. Survey, Reston, Virginia, p. 42.
- Teng F.-Z. (2017) Magnesium isotope geochemistry. *Rev. Mineral. Geochem. Mineral Soc. Am.* **82**, 219–287.
- Teng F.-Z., Li W. Y., Ke S., Marty B., Dauphas N., Huang S., Wu F. and Pourmand A. (2010) Magnesium isotopic composition of the Earth and chondrites. *Geochim. Cosmochim. Acta* **74**, 4150–4166.
- Thomas G. E. (1974) Lineament-block tectonics: Williston-Blood Creek Basin. *Am. Assoc. Petrol. Geol. Bull.* **58**, 1305–1322.
- Thomas W. A. (1985) The Appalachian-Ouachita connection: Paleozoic orogenic belt at the Southern margin of North America. *Ann. Rev. Earth Planet. Sci.* **13**, 175–199.
- Tipper E. T., Galy A., Gaillardet J., Bickle M. J., Elderfield H. and Carder E. A. (2006) The magnesium isotope budget of the modern ocean: constraints from riverine magnesium isotope ratios. *Earth Planet. Sci. Lett.* **250**, 241–253.
- Tóth J. (1978) Gravity-induced cross-formational flow of formation fluids, Red Earth Region, Alberta, Canada: analysis, patterns, and evolution. *Water Res. Res.* **14**, 805–843.
- Vahrenkamp V. C. and Swart P. K. (1990) New distribution coefficient for the incorporation of strontium into dolomite and its implications for the formation of ancient dolomites. *Geology* **18**, 387–391.
- Vahrenkamp V. C. and Swart P. K. (1994) Late Cenozoic dolomites of the Bahamas: metastable analogues for the genesis of ancient platform dolomites. *Spec. Pubs. Int. Ass. Sediment.* **21**, 133–153.
- Wardlaw N. C. (1968) Carnallite-Sylvite relationships in the Middle Devonian Prairie Evaporite Formation, Saskatchewan. *Geol. Soc. Am. Bull.* **79**, 1273–1294.
- Warren J. K. (2000) Dolomite: occurrence, evolution and economically important associations. *Earth Sci. Rev.* **52**, 1–81.
- Wedepohl K. H. (1971) Environmental influences on the chemical composition of shales and clays. *Phys. Chem. Earth* **8**, 305–333.
- Whitaker F. F. and Xiao Y. (2010) Reactive transport modeling of early burial dolomitization of carbonate platforms by geothermal convection. *Am. Assoc. Petrol. Geol. Bull.* **94**, 889–917.
- Wilkinson B. H. and Algeo T. J. (1989) Sedimentary carbonate record of calcium-magnesium cycling. *Am. J. Sci.* **289**, 1158–1194.
- Wilson E. N., Hardie L. A. and Phillips O. M. (1990) Dolomitization from geometry, flow patterns, and the origin of massive dolomite: the Triassic Latemar buildup, northern Italy. *Am. J. Sci.* **290**, 741–796.
- Wittrup M. B. and Kyser T. K. (1990) The petrogenesis of brines in Devonian potash deposits of western Canada. *Chem. Geol.* **82**, 103–128.
- Wombacher F., Eisenhauer A., Böhm F., Gussone N., Regenber M., Dullo W. C. and Rüggeberg A. (2011) Magnesium stable isotope fractionation in marine biogenic calcite and aragonite. *Geochim. Cosmochim. Acta* **75**, 5797–5818.

- Worsham S. R., Holmden C. and Qing H. (2013) Preliminary results of a magnesium isotope study of dolomite in Upper Ordovician strata, southeastern Saskatchewan, northern Williston Basin. *Summ. Rep. Inv. Sask. Geol. Surv.* **1**, 1–8.
- Wright G. N., McMechan M. E. and Potter D. E. G. (1994) Structure and architecture of the Western Canadian sedimentary basin. In *Geological atlas of the Western Canadian sedimentary basin* (eds. G. Mossop and I. Shetsen). Can. Soc. Petrol. Geol. Alberta Res. Council, Calgary, Alberta, pp. 25–39.
- Yapparova A., Gabellone T., Whitaker F., Kulik D. A. and Matthäi S. K. (2017) Reactive transport modelling of hydrothermal dolomitisation using the CSMP++ GEM coupled code: effects of temperature and geological heterogeneity. *Chem. Geol.* **466**, 562–574.
- Zenger D. H. (1996) Dolomitization of the “C” zone, Red River Formation (Upper Ordovician) in a deep core, Williston Basin, Richland County, eastern Montana. University of Wyoming. *Contrib. Geol.* **31**, 57–75.

*Associate editor:* Noah J. Planavsky